

IMPACT OF HEMODYNAMIC PARAMETERS  
ON A STENOTIC AORTIC VALVE: AN IN  
VITRO STUDY

# IMPACT OF HEMODYNAMIC PARAMETERS ON A STENOTIC AORTIC VALVE: AN IN VITRO STUDY

BY MASSOUD EBRAHIMI DEHSHALI, M.Sc.

A Thesis Submitted to the Department of Mechanical Engineering  
and School of Graduate Studies in Partial Fulfilment of the  
Requirements for the Degree Master of Applied Science

McMaster University © Copyright by Massoud Ebrahimi Dehshali,  
September 2022

Master of Science (2022), Department of Mechanical Engineering, McMaster University, Hamilton, Ontario

**TITLE:** Impact of hemodynamic parameters on a stenotic aortic valve: an in vitro study

**AUTHOR:** Massoud Ebrahimi Dehshali, M.Sc.

**SUPERVISOR:** Professor Zahra Keshavarz-Motamed

**PAGES:** xvi, 87

## Abstract

Aortic Stenosis (AS) is a common valve disease, defined as the narrowing of the aortic valve. AS usually occurs together with other vascular and ventricular diseases; leads to insufficient blood supply to the body and adds stress on the heart. This study aims to investigate the impact of hemodynamic parameters on a stenotic aortic valve. Experiments were carried out in a cardiovascular simulator to replicate different physiological conditions. One aortic valve geometry was developed using computed tomography images, with four hypothetical thicknesses: 0.3, 0.6, 0.8, and 1.0 mm. A physiological (non patient-specific) left ventricle volume waveform was applied as the input, and the valves were tested in different physiological conditions to investigate the impact of different parameters on the aortic stenosis.

The effect of artery constriction on AS was evaluated by measuring pressure and flow rate and calculating Effective Orifice Area (EOA) and left ventricle (LV) workload. It was observed that a 49% increase in the Systemic Vascular Resistance (SVR) brings about a 27% reduction in EOA and a 79% increase in left ventricle workload. The coexistence of AS and left ventricle disorder in providing sufficient stroke volume reduces the valve opening area. Experimental results show a 30.5% (0.36–0.25 cm<sup>2</sup>) reduction in EOA when the stroke volume decreases by 50% (60-30 ml). A thicker valve with a higher resistance in turn decreased the EOA and increased the left ventricle workload. The results depict that the LV workload considerably increased with the leaflet thickness (34%). EOA, on the other hand, significantly decreased with the thickness (46.3%). This study highlights that hemodynamic parameters may exacerbate the aortic valve function in patients with AS.

Moreover, to investigate the underlying logics of AS, other coexisting disorders need to be considered.

## Acknowledgments

First, I must express my heartfelt gratitude toward my supervisor, Prof. Zahra K. Motamed, who provided me with enormous support and guided me to accomplish this thesis. Without her invaluable assistance in providing knowledge and expertise, I would have not been able to undertake this journey. I want to extend my gratitude to my committee members, Prof. Chan Y. Ching and Prof. Tohid Didar, for their insights and comments.

I am indebted also to my peers at Motamed Lab for their collaboration and moral support, MohammadAli Daeian and Mohamed Abdelkhalek, for their continuous support and assistance in my tests. I want to thank the mechanical engineering machine shop technicians, particularly Mark Mackenzie, for his precious technical consultations and guidance.

On top of that, my family deserves endless appreciation; without them, this could not have happened. I sincerely thank my parents, Safoura and Alireza, who were my first mentors, and their presence has been heartwarming in all stages of my life. My deepest gratitude goes to my dear wife, Faezeh, for the forbearance, kindness, unconditional love, and sacrifice she has bestowed on me.

# Table of Contents

Abstract .....	iii
Acknowledgments.....	v
Table of Contents .....	vi
List of Tables .....	ix
List of Figures .....	x
List of all Abbreviations and Symbols.....	xiv
Chapter 1 .....	1
1 Introduction and Problem Statement.....	1
1.1 Left side heart anatomy .....	1
1.1.1 Left ventricle .....	4
1.1.2 Heart Valves.....	6
1.2 Aortic Valve Pathology.....	8
1.2.1 Aortic Stenosis .....	8
Chapter 2.....	12
2 Literature Review.....	12
2.1 Cardiovascular simulators.....	12
2.1.1 A review of cardiovascular simulators.....	12
2.1.2 Systemic circulation.....	15
2.1.2.1 Systemic vascular resistance .....	16
2.1.2.2 Systemic compliance .....	17
2.1.2.3 Ventricular pumping and compliance.....	17
2.1.2.4 Dimensionless numbers and similarity.....	18
2.2 Material considerations in in vitro simulations.....	19

2.3 Image Analyses and 3D Model Reconstruction.....	25
2.4 Manufacturing techniques in cardiovascular in vitro simulations .....	28
2.4.1 Molding.....	30
2.4.2 Direct 3D printing.....	32
Chapter 3.....	36
3 Experimental Methods .....	36
3.1 Methods.....	36
3.2 Experimental conditions .....	38
Chapter 4.....	41
4 Results and Analysis .....	41
4.1 Aortic Valves .....	41
4.2 Systemic Vascular Resistance.....	42
4.2.1 The Impact of SVR on the Left Ventricle and Aorta Pressures.....	43
4.2.2 The Impact of SVR on the Effective Orifice Area.....	48
4.2.3 The Impact of SVR on the Left Ventricle Workload.....	49
4.3 Stroke Volume .....	51
4.3.1 The Impact of the Stroke Volume on the Left Ventricle and Aorta Pressure .....	51
4.3.2 The Impact of the Stroke Volume on the Effective Orifice Area .....	55
4.4 Aortic Valve Thickness.....	57
4.4.1 The Impact of the Leaflet Thickness on the Left Ventricle and Aorta Pressures .....	57
4.4.2 The Impact of the Leaflet Thickness on the Effective Orifice Area....	64
4.4.3 The Impact of Thickness on the Left Ventricle Workload .....	65
Chapter 5.....	67

5	Limitations and Conclusion .....	67
5.1	Limitations .....	67
5.2	Conclusions.....	67
	Bibliography .....	70

## List of Tables

Table 1.1 Recommended grading for Aortic Stenosis severity [14] (from Baumgartner et al.) .....	9
---	---

## List of Figures

Figure 1.1 A demonstration of the ventricular function that includes the pressure variations in aorta, atrium, and ventricle, ventricle volume change, ECG and PCG [7].....	4
Figure 1.2 The heart lateral view which illustrates different parts of the left ventricle including the base apex, and free wall [8] (from Whiteman et al.).....	6
Figure 1.3 A visual demonstration of heart valves and their respective locations [11] (from Mayo Clinic website).....	8
Figure 1.4 Normal aortic valve and different types of aortic stenosis [14] (from Baumgartner et al.).....	11
Figure 2.1 (a) A cardiac simulator to test a mitral valve [21] (from Mashari et al.), (b) A porcine left ventricle installed in an in vitro cardiovascular simulator [50] (from Leopaldi et al.). .....	15
Figure 2.2 The diagram illustrates the following: Stress-strain plots of myocardial tissue specimens and corresponding polymeric materials; Stress-strain plots of aortic tissue specimens and corresponding polymeric materials, as well as the calcification material. At small strains (0 to 0.05), a great fidelity can be seen in the stress and strain diagram and the silicone behaviour matches the general trends of human tissue. However, at higher strains, a divergence appears, and the mechanical behaviour of the ink differs noticeably from the tissue [75] (From Haghashtiani et al.). .....	22
Figure 3.1 The schematic diagram of the cardiovascular simulator .....	37
Figure 4.1 Fabricated valve dimensions: four valves of varying thicknesses manufactured through injection molding technique. The valve root diameter is 21 mm, and the valve holder cylinder has a height of 16 mm.....	42

Figure 4.2 Variation of the left ventricular pressure with a gradual increase in systemic vascular resistance for valve #1 in stroke volume of 50 ml. In this test, valve #1 was used, and the systemic vascular resistance was changed using the adjustable resistance component in the cardiovascular simulator. ....44

Figure 4.3 Variation of the aorta pressure with a gradual increase in systemic vascular resistance for valve #1 in stroke volume of 50 ml. In this test, valve #1 was used, and the systemic vascular resistance was changed using the adjustable resistance component in the cardiovascular simulator. ....45

Figure 4.4 A demonstration of the peak-to-peak pressure gradient on the left ventricle and aorta pressure waveforms .....47

Figure 4.5 The impact of systemic vascular resistance on the peak-to-peak pressure gradient of Valve #1 in a stroke volume of 50 ml. ....47

Figure 4.6 The impact of systemic vascular resistance on the Effective Orifice Area (EOA) of Valve #1 in a stroke volume of 50 ml.....49

Figure 4.7 The impact of systemic vascular resistance on the left ventricle workload of Valve #1 in a stroke volume of 50 ml. The left ventricle workload can be computed as  $W = PdV$  where P is the instantaneous left ventricle pressure and V is the corresponding volume.....50

Figure 4.8 Variation of the left ventricular pressure with stroke volume for valve #1. Peripheral resistance and systemic compliance were kept unchanged during the experiments. ....53

Figure 4.9 Variation of the aorta pressure with varying the stroke volumes for valve #1. Peripheral resistance and systemic compliance were kept unchanged during the experiments. ....54

Figure 4.10 The impact of the stroke volume on the transvalvular peak- to-peak pressure gradient for Valve #1. The simulator was tested with stroke volumes of 30 ml, 40 ml, 50 ml, and 60 ml. Peripheral resistance and systemic compliance were kept unchanged during the experiments.....	55
Figure 4.11 The impact of the stroke volume on the effective orifice area (cm <sup>2</sup> ) for Valve #1. The simulator was tested with stroke volume of 30 ml, 40 ml, 50 ml, and 60 ml. Peripheral resistance and systemic compliance were kept unchanged during the experiments. ....	56
Figure 4.12 Variation of the left ventricle pressure with the change in leaflet thickness. Four valves with the same geometry and different leaflet thicknesses were tested in stroke volume of 50 ml. Peripheral resistance and systemic compliance were kept unchanged during the experiments.....	58
Figure 4.13 Variation of the aorta pressure with changes in leaflet thickness. Four valves with the same geometry and different leaflet thicknesses were tested in stroke volume of 50 ml. Peripheral resistance and systemic compliance were kept unchanged during the experiments. ....	59
Figure 4.14 The leaflet thickness impact on the pressure gradient in the constant stroke volume of 50 ml. ....	60
Figure 4.15 Left ventricle pressure, aorta pressure and the peak-to-peak pressure gradient for Valve #1 at stroke volume of 50 ml. ....	61
Figure 4.16 Left ventricle, aorta pressures and the peak-to-peak pressure gradient for Valve #2 at stroke volume of 50 ml.....	62
Figure 4.17 Left ventricle, aorta pressures and the peak-to-peak pressure gradient for Valve #3 at stroke volume of 50 ml.....	63

Figure 4.18 Left ventricle, aorta pressures and the peak-to-peak pressure gradient for Valve #4 at stroke volume of 50 ml.....	64
Figure 4.19 Effective orifice area variations with a change in the thickness of leaflet at stroke volume of 50 ml. ....	65
Figure 4.20 The variation in the left ventricle workload with the change in aortic valve thickness at stroke volume of 50 ml. The left ventricle workload is a function of the left ventricle pressure and volume, and it can be calculated by $WLV = \int P dV$ where P and V are LV volume and pressure, respectively. ....	66

## List of all Abbreviations and Symbols

LV	Left Ventricle
RV	Right Ventricle
LA	Left Atrium
RA	Right Atrium
SVC	Superior Vena Cava
IVC	Inferior Vena Cava
SV	Stroke Volume
AS	Aortic Stenosis
ECG	Electrocardiogram
PCG	Phonocardiogram
AV	Aortic Valve
MV	Mitral Valve
AVA	Aortic Valve Area
PG	Pressure Gradients
SVR	Systemic Vascular Resistance (mmHg.s/ml)
TPR	Total Peripheral Resistance (mmHg.s/ml)

MAP	Mean Arterial Pressure (mmHg)
CO	Cardiac Output (l/min)
C	Arterial Systemic Compliance (ml/mmHg)
VIA	Viscoelastic Impedance Adapter
CNC	Computer Numerical Code
BETV	Bioengineered Trileaflet Valve
FDM	Fused Deposition Modeling
SLS	Selective Laser Sintering
SLA	Stereolithography
CJP	Color Inkjet Printing
MJ	Material Jetting
CT	Computed Tomography
EOA	Effective Orifice Area
$\Delta V$	Change In Arterial Volume (ml)
$\Delta P$	Change In Arterial Pressure (mmhg)
$\alpha$	Womersley Number
$\omega$	Angular Frequency of The Pulse Wave (radians/sec)
$\vartheta$	Kinematic Viscosity (m <sup>2</sup> /S)

$r$	Radius (m)
$Re$	Reynolds Number
$\rho$	Density ( $\text{Kg/m}^3$ )
$V$	Mean Velocity (m/s)
$\mu$	Dynamic Viscosity (Pa.s)
$D$	Characteristics Length (m)
$d$	Distensibility (1/Pa)
$E$	Young's Modulus ( $\text{N/m}^2$ )
$\lambda$	Propagation Wavelength (m)
$s$	Wall Thickness (mm)
$q_v$	Volumetric Flow Rate (ml/s)

# Chapter 1

## 1 Introduction and Problem Statement

### 1.1 Left side heart anatomy

The cardiovascular system is responsible for distributing nutrients and oxygen to tissues in the body and allows for the removal of carbon dioxide and waste products. In addition to assistance with respiration, this system assists with other vital functions such as transporting immune cells for protection. The cardiovascular system consists of the heart, arteries, veins, capillaries and the blood that is pumped to the entire body [1].

The human heart is comprised of four muscular chambers, including the Left Ventricle (LV), Right Ventricle (RV), Left Atrium (LA), and Right Atrium (RA). A septum physically separates the left and right sides of the heart, and blood passes through the structures at different points in the cardiac cycle. The heart pumps deoxygenated blood from the body to the right atrium through the superior vena cava (SVC) and inferior vena cava (IVC). The blood is then pumped to the lungs to get reoxygenated and returns to the left side of the heart. The left side of the heart is responsible for pumping oxygenated blood to the body tissue. The heart chambers are separated by a wall of tissue, with a serosal layer filled with pericardial fluid and a strong fibrous layer. The structure of these separations allows the heart to minimize friction and optimize energy usage. Additionally, the thickness of these structures varies in the heart, with ventricle walls being thicker than atrial walls.

Moreover, the left side of the heart is larger and thicker than the right due to its function, as it must pump blood further around the body and with increased resistance [2]. The lungs play a key role in respiration, in which they exchange carbon dioxide from the heart with oxygen from the lungs. This allows for the pulmonary veins to transport oxygenated blood to the left atrium. The oxygenated blood passes the mitral (bicuspid) valve to the left ventricle and is pumped through the aortic valve to the body. The aorta has various branches allowing for the distribution of oxygenated blood to all body parts and organs. This is attributed to the blood circulation from the heart to the body that is called systemic circulation [3].

The cardiac cycle describes the various stages of blood circulation that occur in the duration of one heartbeat. The cardiac cycle has two distinctive parts, a period of contraction called systole and a period of relaxation called diastole [4]. When ventricular pressure surpasses the pressure within the pulmonary artery or aorta, the blood is pushed out of the ventricular chamber and past the given semilunar valve (Aortic valve and pulmonary valve). During systole, the atrial pressure is less than ventricular pressures, causing the atrioventricular valves (mitral valve and tricuspid valve) to remain closed. The relaxation of ventricular myocytes results in a decrease in ventricular pressure, causing the atrial pressure to be greater in comparison. This phase is ventricular diastole, where the atrioventricular valves open, allowing the ventricles to refill. During diastole, the semilunar valve remains closed due to increased arterial pressures in the aorta and pulmonary arteries, which exceed the interventricular pressures [5].

A series of mechanical and electrical events assist in explaining blood flow during the cardiac cycle. Figure 1.1 displays the mechanical events of the cardiac cycle in detail. An Electrocardiogram (ECG) displays the electrical activity of the heart throughout the cardiac cycle. This is a vital tool used for diagnostic purposes, allowing for the diagnosis of various heart disorders. A phonocardiogram (PCG) is another useful instrument that detects the vibrations caused by valve closures and records heart sounds [6]. The cardiac cycle is divided into four phases, based on the closures of the heart valves. These phases are [7]:

Phase I: The Filling Period – The atrioventricular valves are opened, the semilunar valves are closed during this phase, and the opening of the inlet valve allows for ventricular filling.

Phase II: Isovolumetric Contraction – Both atrioventricular valves and semilunar valves are closed during this phase, and the pressure increases while the blood volume remains constant.

Phase III: Ejection Period – The semilunar valves are opened, and the atrioventricular valves remain closed. Due to increased contractions, blood pressure rises during this phase.

Phase IV: Isovolumetric Relaxation – Both atrioventricular valves and semilunar valves are closed, and the intraventricular pressure decreases while the blood volume remains constant.

Figure 1.1 depicts the events of the cardiac cycle for the left side of the heart for two complete cycles. This image denotes the blood volume and pressure at certain events. The

pressure changes of the aorta, left ventricle, and left atrium are illustrated by the top three curves. The fourth curve (blue) displays the left ventricular blood volume throughout the cycle, the fifth curve denoted the ECG curve, and the sixth curve illustrates the PCG curve [7].

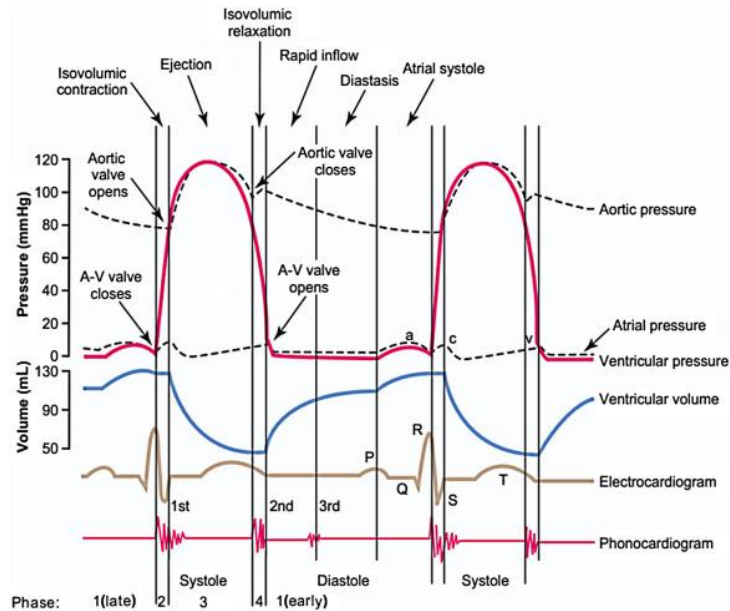


Figure 1.1 A demonstration of the ventricular function that includes the pressure variations in aorta, atrium, and ventricle, ventricle volume change, ECG and PCG [7]

### 1.1.1 Left ventricle

The structure of the left ventricle, which acts as a pump for systemic circulation, is conical in shape, is longer, has thicker walls (compared with the right ventricle) and has an anteroinferior projecting apex. The apex of the left ventricle is often located in the fifth left intercostal space and is the anatomical apex of the heart. This structure is separated from

the right ventricular apex by the interventricular septum, and it is covered by the left lung. The apex of the heart is often used as an entry point into the left ventricle for valvular therapies. This is due to the relative thinness of the myocardium at this location, allowing it to be used to insert devices, tubes, and electrodes. However, this increases the risk of perforation of the left ventricle during surgical processes. The base of the left ventricle begins along the atrioventricular groove to the papillary muscles within the ventricle. The atrioventricular groove and posterior coronary sinus superficially separate this structure from the left atrium. Free wall is a structure of the left ventricular wall that does not touch the apex or interventricular septum. The myoarchitecture of the left ventricle is from the atrioventricular junction to the ventriculoarterial junction. At its maximum thickness, the left ventricular wall is three times thicker than the right wall at around 12-15 mm. The myocytes of the heart chambers are arranged to create a 3D network of conjoining fibers, caused by the myocyte branches that adjoin neighboring myocytes (Figure 1.2) [8].

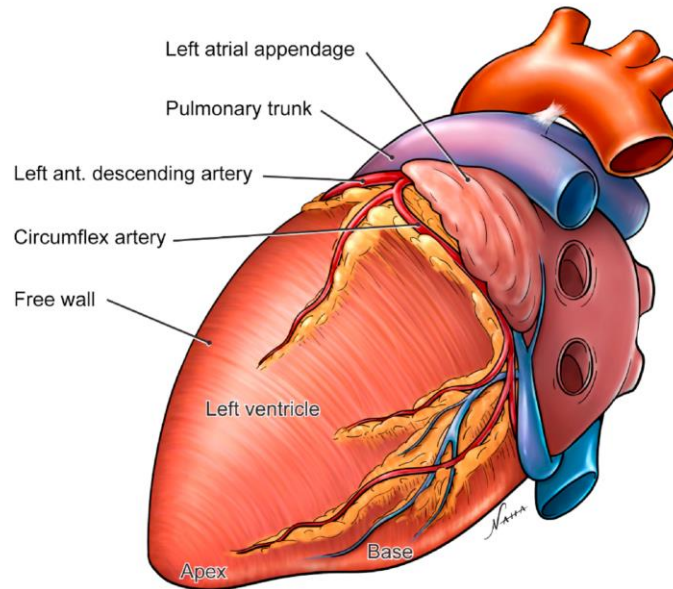


Figure 1.2 The heart lateral view which illustrates different parts of the left ventricle including the base apex, and free wall [8] (from Whiteman et al.)

### 1.1.2 Heart Valves

The aortic valve (AV) (Figure 1.3) is a semilunar valve that contains three leaflets or semilunar cusps. A fibrous ringed structure is implanted in the intraventricular septum and attaches the valve cusps together. The leaflets of the AV are bordered with endothelial cells and contain a “dense collagenous core adjacent to the high-pressure aortic side” [9]. Fibrosa is the major fibrous layer of the leaflet, and it is on the adjacent side of the aorta. The ventricularis is the layer that conceals the ventricular side of the aortic valve. This layer contains elastin and collagen fibers. There is a physical separation between the aorta and left ventricle, being the fibrous annular ring. The superior region of this ring contains the

sinus of Valsalva (the aortic sinus). This structure contains three protrusions at the base of the aorta, and each protrusion is aligned with the specific valve leaflets [9].

The mitral valve (MV) is the atrioventricular valve on the left side of the heart. This structure helps impede blood flow backwards with its complex structure. The MV contains a sub-valvular apparatus which is created by chordae tendineae and papillary muscle. A fibrous ring called the annulus outlines the outer circumference of the valve, securing it to the left side of the heart. The annulus is adjacent to the AV and is continuous with aspects of the aortic annulus. This is a dynamic structure, as it varies in shape and diameter during the cardiac cycle. During ventricular systole, the annulus has a saddle shape assisting the closure of the valve, whereas in diastole it is more circular in shape. The MV leaflets are attached to the annulus and are a continuous extension of tissue [10].

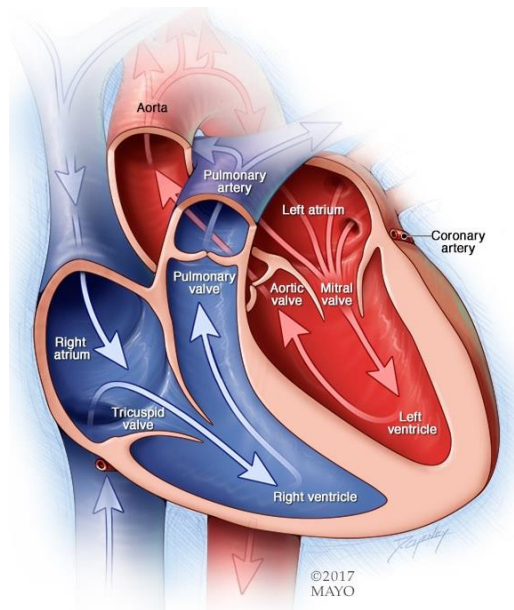


Figure 1.3 A visual demonstration of heart valves and their respective locations [11]  
(from Mayo Clinic website)

## 1.2 Aortic Valve Pathology

### 1.2.1 Aortic Stenosis

Aortic stenosis is a common disorder in which there is a blocking or narrowing of the valve opening. Often, this is idiopathic and leads to further degeneration and calcification of the valve leaflets. This condition may be inevitable for those who are born with a bicuspid aortic valve, which is prone to aortic stenosis. There is a lot of variation in the progression of this condition, and if an artificial replacement valve is not employed, almost 75% of the patients die within three years [12].

The aortic valve area (AVA) and the pressure gradients (PG) between the aorta and left ventricle are used to measure the severity of aortic stenosis. Following the calculations of these metrics, stenosis can be classified as mild, moderate, severe, or critical [13]. The hemodynamic severity of the aortic stenosis should be considered to assess the severity, and it does not exactly correlate with the signs and symptoms of the disease (Table 1.1). A classification of aortic stenosis which uses the aortic valve opening area and hemodynamic severity for critical cases is given by Table 1.1 as a guide to grade the AS [14]. Studies indicate that aortic stenosis is usually a self-maintaining and slowly progressive condition, however, rare cases show that mild to severe aortic stenosis can occur within a few years [15].

Table 1.1 Recommended grading for Aortic Stenosis severity [14] (from Baumgartner et al.)

	Aortic sclerosis	Mild	Moderate	Severe
Peak velocity (m/s)	$\leq 2.5$ m/s	2.6–2.9	3.0–4.0	$\geq 4.0$
Mean gradient (mmHg)	–	$< 20$	20–40	$\geq 40$
AVA (cm <sup>2</sup> )	–	$> 1.5$	1.0–1.5	$< 1.0$
Indexed AVA (cm <sup>2</sup> /m <sup>2</sup> )	–	$> 0.85$	0.60–0.85	$< 0.6$
Velocity ratio	–	$> 0.50$	0.25–0.50	$< 0.25$

Aortic stenosis can be classified with dyspnea and symptoms of angina, heart failure and syncope. Additionally, the presentation of the symptoms may vary between patients and present more subtly or critically [16]. Aortic stenosis is attributable to the following causes (Figure 1.4) [17]:

### **Calcific aortic stenosis**

The initial stage of aortic stenosis is like coronary artery disease, with various common risk factors including, age, sex, hyperlipidemia and active inflammation. It is also a common occurrence for an individual to develop both disorders in their lifetime. The main cause of calcified aortic stenosis is the accretion of solid calcium deposits on the aortic valve cusps. This results in the release of inotropic agents and vasodilators to increase cardiac output. Babies can also be born with a bicuspid aortic valve, which is more susceptible to aortic valve stenosis compared to tricuspid valve. In a quantitative sense, unlike diseased tricuspid valves which take six to eight decades to develop stenosis, stenosis in a bicuspid aortic valve can occur in two decades.

### **Congenital aortic stenosis**

Inborn aortic stenosis is called congenital aortic stenosis and comes with different severity. Severe cases of congenital aortic stenosis are diagnosed and treated in the initial stages of life, however, there are cases where it may be undiagnosed until adulthood. This disorder is often characterized by a unicuspidal valve or a bicuspid valve. Children with this condition often die or develop symptoms that lead to diagnosis and valve replacement. It

is common for asymptomatic individuals to suddenly die with this condition in comparison to developing heart failure or angina. This can be attributed to the increased ejection performance and subnormal wall stress, caused by hypertrophy that compensated for the increased pressure overload.

### **Rheumatic valve disease**

Rheumatic fever is a rare cause of aortic stenosis in developed countries. This type of aortic stenosis invariably affects the mitral valve and cannot be diagnosed without an echocardiogram indicating mitral valve deformity. Additionally, in contrast with calcified aortic stenosis a commissural fusion is often present with this disorder.

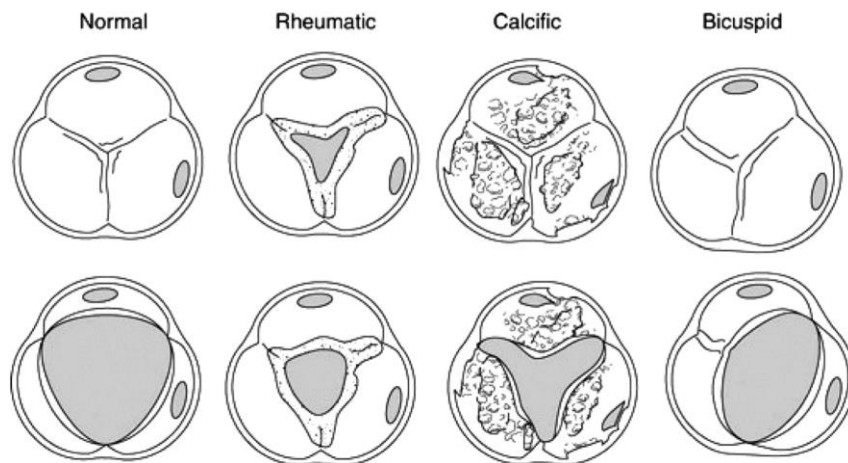


Figure 1.4 Normal aortic valve and different types of aortic stenosis [14] (from Baumgartner et al.)

# Chapter 2

## 2 Literature Review

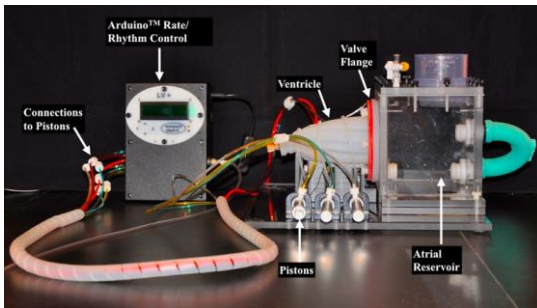
### 2.1 Cardiovascular simulators

#### 2.1.1 A review of cardiovascular simulators

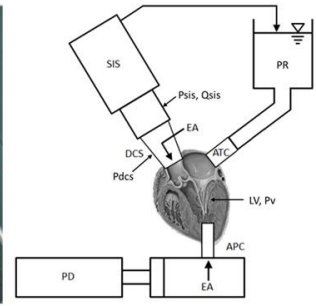
Since the invention of the preliminary pulse duplicators [18]–[20], many efforts have been made to improve their generated waveforms and applicability in cardiovascular research. In this part, the in vitro cardiovascular simulators are classified under three main categories based on the purpose of the study, which include (1) mitral valve investigation, (2) aortic valve and aorta investigation, and (3) left ventricle investigation. To begin, some studies designed in vitro cardiovascular simulators specifically for mitral valve flow investigation [21]–[24]. For instance, Mashari et al. [21] designed a circulation system to test a mitral valve that was placed between an atrial reservoir and a ventricular chamber (Figure 2.1-a). The left atrial reservoir was open to atmospheric pressure which provided the lower atrial pressure. The mitral valve was tested under different LV pressure ranges, achieved through a combination of springs along with an adjustable threaded screw on top of the connected tower [23]. The volume of the left ventricle was altered using a series of pistons powered by an air compressor, which simulated diastolic filling across the mitral valve. Despite its

potential, the in vitro cardiovascular simulator was specific to only the diastolic phase of the cardiac cycle, preventing the analysis of the systolic phase. Alternatively, some researchers have designed pulse duplicators that were limited to the investigation of the aortic valve and the systolic phase of the cardiac cycle [25]–[32]. For aortic valve investigation, an aortic valve and sinus chamber are installed into the aortic position of a left heart simulator. Lastly, for more general studies, the entire left ventricle, including both the mitral valve and aortic valve are considered in the geometry when studying flow hemodynamics [33]–[44]. For example, Papolla et al. [34] designed a left heart in vitro simulator using elastic silicone models of the LV, ascending aorta and left atrium (LA). In these types of in vitro cardiovascular simulators, a rigid transparent box (acrylic) is designed to house the silicone model of the LV. The box is coupled to a piston pump which translates the reciprocating motions of the piston to the contraction and expansion of the LV chamber [40]. In order to achieve a more physiological waveform and boundary condition, the LV box is coupled with a viscoelastic impedance adaptor. This device consists of compliance chambers and resistance to model the left ventricle impedance [45]. The pump is generally capable of producing both E and A waves [46], [47], however, the contraction and expansion of the left atrium are sometimes generated using a second active system. An example of a second active system includes a servomotor acting on a cam-follower mechanism in direct contact with the LA outer surface [40]. In the study conducted by Papolla et al. [34], the in vitro cardiovascular simulator operated using a linear motor, which activated the piston to create a physiological mitral inflow which

included both E and A waves. They designed a mechanism to adjust the tension of chordae tendineae and then tested the system under various pressure and flow conditions. The use of a compliant left ventricle chamber provides a more accurate analysis of flow dynamics and their impact on heart valves [33], [48]. Some simulators use real heart chambers and valves, coupled to a Windkessel system that mimics the heart hemodynamics in vitro [49], [50]. For instance, Leopaldi et al. [50] connected a piston pump – capable of generating both systolic and diastolic waveforms – to a porcine LV apex (Figure 2.1-b). This device was connected to a hydraulic circuit design based on a classical three lumped parameter model (RCR), i.e., a characteristic resistance, a capacitance, and a peripheral resistance. The LV chamber was modified to facilitate a sealed connection to the pulse duplication system and hydraulic piping system [50]. Furthermore, commercial in vitro cardiovascular simulators have been manufactured by several companies such as ViVibro, BDC, Archetype Medical Inc, and Dynatek. Although these devices offer easier control and more automated systems, they lack flexibility to study a range of diseases and their conditions.



(a)



(b)

Figure 2.1 (a) A cardiac simulator to test a mitral valve [21] (from Mashari et al.), (b) A porcine left ventricle installed in an in vitro cardiovascular simulator [50] (from Leopaldi et al.).

### 2.1.2 Systemic circulation

In order to develop a physiological in vitro study, the manufactured phantom must be installed into a circulation system which produces physiological blood flow conditions. Generally, a cardiovascular simulator consists of a resistance, a compliance, a ventricular pumping system, connecting pipes and a hydraulic system [51]. The physiological flow conditions generated in the in vitro circulation should be monitored at critical points along the system to ensure a proper waveform generation. To achieve this, the in vitro set up must be customized to enable specific measurement techniques that can quantify human heart hemodynamics and metrics, such as velocity fields and pressure variations. In vitro cardiovascular simulators (Pulse Duplicators) are designed to monitor flow changes at key points along the system and are equipped with a variety of sensors and transmitters that can measure pressure, flow [25], displacement [28], and force [34], [52]. The pump, piping system and the hydraulic elements must be chosen to replicate human flow features and characteristics by considering the pulsating nature of blood flow and elastic behaviour of the vessels.

### 2.1.2.1 Systemic vascular resistance

Systemic vascular resistance (SVR), or total peripheral resistance (TPR), is an important factor for evaluating circulatory function and represents the resistance to blood flow due to the vasculature in systemic circulation. In left heart modeling, SVR is a key factor that must be considered when designing the circulation components. SVR is highly dependent on vessel diameter and blood viscosity within the circulatory system. Vessel diameter is controlled by the activity of smooth muscle found in the walls of blood vessels; contraction of these muscles (vasoconstriction) increases SVR, and relaxation of these muscles (vasodilation) decreases SVR [53].

SVR typically ranges from 1.0 to 1.2 mmHg.s/mL [54] and, in an in vitro cardiovascular simulator, can be modeled by a simple hydraulic valve [55], [56], a porous medium [20], or a clamp. As seen in Equation 2-1, SVR can be approximated using Ohm's Law [54], [57], where MAP represents the mean arterial pressure, and CO is the cardiac output [53], [54]. The units used in an in vitro cardiovascular simulator for resistance, pressure, and cardiac output are generally mmHg.min/L, mmHg and L/min, respectively. Like an electrical circuit, the resistances imposed by the arterial system can be arranged in series or in parallel. When the resistors are arranged in series, the sum of individual resistive components provides the total resistance. Alternatively, when the resistors are arranged in parallel, the sum of the reciprocals of the individual resistive components provides the total resistance [54], [57].

$$SVR = \frac{MAP}{CO} \quad 2-1$$

### 2.1.2.2 Systemic compliance

Vascular compliance defines the ability of a vessel to sustain changes in blood volume and pressure through contraction and expansion. Compliancy is an important feature of the cardiovascular system as it acts as protection against dramatic rises in systolic blood pressure [58]. Without proper compliance, a cardiovascular system suffers from undesired increases in systolic blood pressure and decreases in early diastolic blood pressure [58]. Equation 2-2 [58] can be used to calculate arterial systemic compliance (C) in mL/mmHg, where  $\Delta V$  and  $\Delta P$  represent the change in arterial volume in ml and the change in arterial pressure in mmHg, respectively.

For an in vitro cardiovascular simulator, arterial systemic compliance can be modeled using a Windkessel chamber or any elastic chamber. The Windkessel chamber is partially filled with a blood mimicking liquid as well as air which is compressed (during diastole) or expanded (during systole) to simulate the systemic compliance [54].

$$C = \frac{\Delta V}{\Delta P} \quad 2-2$$

### 2.1.2.3 Ventricular pumping and compliance

The heart acts as a positive displacement pump that pushes blood throughout the body with each expansion and contraction. The pumping action of the heart is based on a physiologic

waveform that follows a cyclic movement [59], [60]. In an in vitro cardiovascular simulator, a pump (such as a piston pump, a bladder pump, etc.) is often used to simulate the ventricular function of the heart, which is coupled to an elastic LV sac that is immersed in a box or tank (usually transparent) [61]. The displacement pump causes movement of the LV chamber (or sac) which generates the systolic and diastolic phases of the cardiac cycle. In a physiologic case, the accurate ventricular pumping action and compliance are achieved through the proper combination of the LV chamber, the pump configuration and its generated waveform [62].

In order to duplicate the LV wall material properties and its impact on the LV pressure during expansion and compression, a Viscoelastic Impedance Adapter (VIA) is designed along with the piston pump to generate a realistic physiological pressure in the LV [63], [64]. The thin-walled LV responds to the expansion-contraction in a different way compared to the real LV. To compensate for this discrepancy, the VIA is coupled with the pump and LV system to simulate the ventricular distensibility [65]. In general, VIA is a pressure vessel partially filled with water and air, and an adjustment in the air and water ratio leads to a desired ventricular distensibility [66].

#### 2.1.2.4 Dimensionless numbers and similarity

To achieve an ideal physiological condition, the simulated circulatory system needs be dynamically similar to the human heart. The dynamic similarity of the in vitro system can be confirmed by checking two dimensionless numbers: Womersley number and Reynolds

number. The Womersley number characterizes pressure and velocity profile variations, as well as the pulsating nature of flow in the cardiac cycle. The Womersley number defines the ratio of unsteady inertial forces to viscous forces in the flow, where  $r$  represents the radius of the tube,  $\omega$  is the angular frequency of the pulse wave (heart rate expressed in radians/sec), and  $\nu$  is the kinematic viscosity, as shown in Equation 2-3 [67].

$$\alpha = r \sqrt{\frac{\omega}{\nu}} \quad 2-3$$

Furthermore, the Reynolds number is used to differentiate between laminar and turbulent flow, where  $\rho$ ,  $V$ ,  $\mu$ , and  $D$  represent the density, mean velocity, dynamic viscosity of the fluid, and the characteristics length, respectively, as shown below in Equation 2-4.

$$Re = \frac{\rho V D}{\mu} \quad 2-4$$

Based on this calculation, laminar flow is described by a Reynolds number below 2100, while a Reynolds number greater than 2100 results in a transition from laminar to the turbulent regime.

## 2.2 Material considerations in *in vitro* simulations

The 3D printed organs used in an *in vitro* cardiovascular simulator should exhibit material properties similar to human tissues. Many factors including disease states, age, position and orientation of tissue excisions vary from case-to-case and are heavily influential on organs' material properties. The mechanical properties of cardiac tissues that must be considered

include consistency, elasticity, tensile strength, tear resistance and memory capacity [68], [69]. For instance, to properly replicate the cyclic movement of the heart overtime in an *in vitro* experiment, it is crucial to remain within the elastic range of the material. This can be accomplished by testing the material to derive its stress-strain curve [70].

In order to choose a material best suited for cardiac simulations, a set of criteria has been developed and is frequently used by cardiovascular researchers. Two significant criteria used when selecting a material for a thin-walled model are distensibility and propagation length. Distensibility ( $d$ ) defines the fractional change in cross-sectional area ( $A$ ) of a segment of a material with Young's modulus ( $E$ ), as seen in Equation 2-5.

$$d = \frac{1}{A} \frac{\Delta A}{\Delta p} = \frac{1}{E(h/D)} \quad 2-5$$

Propagation length ( $\lambda_{model}$ ) represents the longitudinal response of the vessel wall. Specifically, for the accurate analysis of the effect of compliance there is a required model length ( $L_{model}$ ) which should be matched to real-world values [71] of length ( $L_{RW}$ ) and real-world values of propagation wavelength ( $\lambda_{RW}$ ), as seen in Equation 2-6.

$$\frac{L_{model}}{\lambda_{model}} = \frac{L_{RW}}{\lambda_{RW}} \quad 2-6$$

In addition to the above criteria, it is essential to replicate tissue compliancy and strength. Proper replication of tissue compliancy allows a model to accurately simulate the ability of the heart to withstand continuous rhythmic deformations [72]. By choosing the proper thickness and material, the compliancy can be appropriately adjusted. To elaborate, for a

specific material with elastic modulus  $E$ , and a fixed geometric size, we can find the proper thickness ( $s$ ) to reach the desired compliance ( $C$ ) using Equation 2-7, where  $l$  represents the length of the considered tract, and  $r$  is the internal lumen radius [73].

$$s = \frac{2\pi lr^3}{EC} \quad 2-7$$

To achieve a convergence between the mechanical properties of artificial materials and human tissue, many compositions of materials have been tested. When developing an ideal ink for a phantom, there are several material property requirements that must be satisfied. These requirements include adjustable properties, good printability, maintaining stable structures and properties during and after printing, etc. [74]. Silicone is frequently used for the manufacturing of compliant structures as silicone agents can be used to harden a rubber mixture (with an active agent) or add flexibility (with a bulking agent). An additive agent may also be used for fine-tuning of color and/or printability. Adjusting the weight ratio of silicone can lead to a wide range of mechanical properties which can be tailored to replicate human tissue behaviour. Figure 2.2 shows the relationship between the mechanical behaviour of human tissues and tailored polymeric materials. In small strain ranges, there is a satisfactory agreement between the materials, however, as strain ranges increase, a significant divergence between the stress-strain curves of polymeric materials compared with tissue specimens can be observed [75].

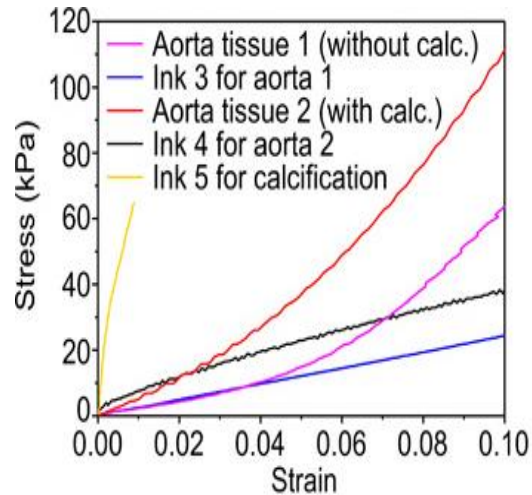


Figure 2.2 The diagram illustrates the following: Stress-strain plots of myocardial tissue specimens and corresponding polymeric materials; Stress-strain plots of aortic tissue specimens and corresponding polymeric materials, as well as the calcification material. At small strains (0 to 0.05), a great fidelity can be seen in the stress and strain diagram and the silicone behaviour matches the general trends of human tissue. However, at higher strains, a divergence appears, and the mechanical behaviour of the ink differs noticeably from the tissue [75] (From Haghiastiani et al.).

With the incredible advancements in material science throughout years of research, many tissue mimicking materials have been created that aim to satisfy the criteria mentioned above. Tissue mimicking materials demonstrate a biological and viscoelastic behaviour, similar to human tissue. Some of these materials include biopolymers and synthetic polymers. By tailoring the features of these materials, human tissue properties can be replicated depending on the application [76]. Unfortunately, many of the tissue mimicking materials present their own limitations. For instance, hydrogel-based tissue mimicking

materials are prone to water evaporation and bacterial growth, leading to short model lifetimes [77].

Researchers often consider different factors when selecting materials to be used in their research based on specific study requirements and desired results. Accurate flow visualization is a common challenge presented when designing a phantom. To overcome this, researchers often consider both mechanical properties and transparency when selecting a material. For better flow visualization, it is sometimes preferred to use a rigid material and sacrifice compliancy [78]. For example, Moore and Dasi [25], [26], [79] mounted a porcine bioprosthetic aortic valve inside a clear, acrylic sinus chamber, machined to mimic the geometry of the outer walls of the aorta. Acrylic is a rigid material that cannot replicate the elasticity of human tissue [80]. In order to obtain both transparency and compliancy, silicone is widely used to fabricate phantoms and perform optical diagnostics [33], [81]–[84]. In addition to elasticity and compliance, the geometrical properties (such as wall thickness) play a crucial role in phantom fabrications. Although using elastic materials can better exhibit pathology compared to other materials, they cannot guarantee the realistic or physiological material response. Furthermore, some researchers use Polydimethylsiloxane (PDMS), which has a similar elastic behaviour to rubber and through molding techniques, can be used to fabricate compliant models. In this regard, Zhang [84] used a PDMS aortic root to compare two prosthetic aortic valve models, both of which had stenosis. The model was transparent and elastic to accommodate the phase-locked PIV, and simulate tissue compliancy, respectively. However, the model had a general geometry with a uniform

thickness, and therefore was not realistic. To the best of our knowledge, no previous models have validated the distensibility or reproduction of real tissue properties. Some material properties such as surface roughness of the coronaries and chordae tendineae have not been considered in most studies. In order to see these details and their impacts, Hatoum et al. [27] designed a compliant aortic root which considers the coronary arteries and any obstructions. Despite the benefits of this model, this phantom had a uniform thickness, and was not manufactured with a realistic tissue compliance. Mashari et al. [21] designed a mitral valve based on geometry with chordae tendineae replicated using braided fishing thread, and deployed it inside a cardiovascular simulator. Although this model shows some potential, it is unlikely that the braided fishing thread is an ideal material to accurately mimic human tissue behaviour. Furthermore, the accuracy of the location and arrangement of the chordae tendineae are dependent on the imaging techniques and are required for a realistic approach.

Various materials are commonly used in the manufacture of cardiovascular models for clinical training and research. Current models use rigid-plastic materials, rubber-like materials, and powder-based materials. It is essential to choose a material that can properly mimic the mechanical properties of human tissue when performing an in vitro study. This will result in a more accurate representation of human heart behaviour. Although there are ongoing studies to develop materials similar to human tissue, available materials can be selected based on mentioned criteria to optimize the function of the model from a material features perspective.

There are many other in vitro simulators which was used to investigate the impact of hemodynamics of the vascular diseases in the literature, e.g., [31], [85], [86]. Such studies are not the scope of this thesis.

## 2.3 Image Analyses and 3D Model Reconstruction

To study the anatomical variations and their influence on hemodynamics, a physiological geometry must be considered. Generating anatomical geometry and a 3D model involves the following processes: (1) acquisition of image data in the form of DICOM Data, (2) cropping and extracting the regions that are going to be studied, (3) transforming the segmented part to a 3D mesh generator software to prepare the required file for 3D printing and improving its topology, and (4) transferring the final file to a 3D printer and printing it [87], [88].

### **(1) Acquisition of image data from DICOM data**

For anatomy modeling of cardiovascular mechanics, there are non-invasive imaging techniques (such as CT, MRI, 3D ultrasound) or an invasive method combining catheterization and intravascular ultrasound. Amongst different imaging modalities, echocardiography offers a low-cost modality with a relatively higher temporal resolution. Echocardiography enables us to select the optimal timing but has a narrow field of view [89], a low signal to noise ratio, and many artifacts from bones and air [69], which may maximize the error and lower the reproducibility [90].

Although modalities such as ultrasound can be deployed to acquire the image data [91]–[93], MRI and CT are the most popular and widely used modalities [94]–[96]. One method for capturing and generating anatomical geometry is to use MRI, which provides 2D grey-scale images in DICOM format, in which each image pixel intensities corresponds to different tissue density [97], [98]. MRI data has a limited resolution together with noises, and some smoothing and interpolations are used to make it possible to generate the geometry. MRI is a time-consuming method, and any tiny movement of the patient will result in inaccurate imaging and loss of contrast [71]. Most researchers use CT imaging which has a higher contrast [77], [99], [100] and provides a spatial resolution of 0.3–0.7 mm. To enhance the imaging resolution and have a clearer geometric detail, a contrast agent –such as a specific volume of iodine contrast –is usually injected into the bloodstream of the patient [101].

There are some criteria to choose the best images for the geometry reconstruction. The suitable pixel size and slice thickness need to be selected based on the size of the structures that we aim to generate 3D-models for. In other words, the minimum pixel size and slice thickness should be selected to be able to visualize the smallest features of interest [102]. Additionally, choosing the proper form of images is of importance from the manufacturing perspective. Consequently, some forms such as volume rendered images cannot be chosen for 3D printing and manufacturing purposes. On the contrary, surface rendered images, with contours that sharply define the object by using Hounsfield unit iso-contours and can be converted to a mesh, are perfect for 3D printing [103].

## **(2) Cropping and extracting the regions that are going to be studied**

After acquiring the imaging data, it needs to be processed for 3D model creation and printing, through a technique called segmentation. Segmentation involves dividing the outer surface of the images into regions based on the properties of the area [103]. In this process, the images are partitioned into multiple regions of objects and boundaries. The movement of the myocardium and the blood flow result in some difficulties in performing the segmentation, which leads to a need for an extremely complex network to learn. The segmentation algorithm is chosen based on a balance between the complexity, the time required, and the segmentation results [104]. The methods commonly used for heart chamber segmentation are edge detection, region-based segmentation, and pixel classification [105]. Segmentation requires a commercial software or a freeware, which enables the distinction between different tissues and the identification of boundaries. Each segmentation software follows a series of steps namely: (1) cropping the area of interest, (2) adjusting the range of Hounsfield unit values to enhance contrast, (3) removing the undesirable parts, and (4) generating the appropriate output file format for 3D printing including STL (Standard Tessellation Language), VRML (Virtual Reality Modeling Language), AMF (Additive Manufacturing File Format) and OBJ (Object) [69], [102]. It should be noted that the values of the threshold in Step 2 are adjusted to extract the entire desired parts. Inevitably, this will result in unwanted anatomical structures with similar grayscale level in the image, and consequently, Step 3 is required to remove these parts [70]. Image voxel size and reconstruction kernels are important parameters and need to be

determined depending on the requirements. If subtle details are interested, small voxel size and sharp kernels are appropriate, requiring more manual segmentation and post-processing. On the other hand, if there is no need for tiny details, larger voxel size and ‘soft’ reconstruction kernels can be used, which may enable automatic segmentation [103].

### **(3) Transforming the segmented part to a 3D mesh generator software to prepare the required file for 3D printing and improving its topology**

Following the segmentation, the 3D model can be manipulated or refined more using limitless computer-aided design tools. The primary reasons for this manipulation include repairing the errors and discontinuities, such as holes, in the segmented model, smoothing to ameliorate the original image resolution, and appending the part to other parts by combining them [106]. Currently, imaging modalities impose limitations on the path to precise studies. The temporal and spatial resolutions are lower than that required for generating appropriate models for 3D printing of fine moving structures, such as valve leaflets and chordae tendinea [69]. Once the final file is ready, it is sent to a 3D printer to be constructed.

## **2.4 Manufacturing techniques in cardiovascular in vitro simulations**

After generating the geometry and determining the appropriate material properties, an applicable manufacturing technique must be selected. Manufacturing techniques

commonly used in the fabrication of cardiovascular simulators include machining, injection molding, and 3D printing. Selecting the proper manufacturing technique is highly dependent on the chosen material and complexity of the geometry. Depending on the purpose of the study, several simplifications may be used when developing the cardiac simulator. For instance, studies which provide a basic understanding of blood flow and hemodynamics have simplifications integrated into the design including steady flow conditions, a fixed diameter tube, simplified disorders (such as a symmetric stenotic geometry), rigid tubes (by neglecting natural compliance), and continuous flow (by eliminating flow pulsations) [107], [108].

The simplifications used in cardiovascular simulators are heavily influential on the manufacturing method and can be used to determine the most effective technique. Machining is a common technique chosen to manufacture phantoms made of rigid materials (such as acrylic) and can be appropriately used for models that neglect the mechanical properties of heart tissue, such as natural compliance. Although these simplifications provide benefits in terms of the manufacturing and basic understanding of the simulator, they present many limitations to the study. In order to design cardiac simulators that are applicable in clinical research, there is a need to manufacture phantoms using flexible materials that exhibit tissue-like behaviour. In this section, I will briefly explain injection molding and direct 3D printing, which are the most common techniques used to produce flexible cardiovascular simulators and have the potential to generate physiological models.

### 2.4.1 Molding

Injection molding is a common method used to generate human organs with materials capable of mimicking human tissue properties. When performing this technique, the chosen material is injected into a mold, and the desired geometry is achieved through a casting process [109]–[111]. When constructing organs, the molds are often 3D printed using physiological measurements [76]. Two injection molding techniques are commonly used when 3D printing the molds. The first method involves injecting a tissue mimicking material into a negative (or female) 3D printed mold [112]. The second method involves using a rigid, positive (or male) 3D printed mold of the organ to generate a negative mold, which is then infused with a compliant material, such as silicone, polyurethane or other tissue mimicking material [113], [114].

Although injection molding is a very useful technique to manufacture cardiovascular phantoms, in complex geometries, it can result in model irregularities. A post-processing method is often required to smooth surfaces and achieve optimal model fidelity to repair any deviations in the model. In order to achieve the proper thickness, the pouring-draining-drying process must be repeated to generate several layers of material [115].

Molding has been widely used in clinical research to manufacture heart components such as heart chambers [61], [116]–[120], heart valves [121]–[124] and blood vessels [109], [125]–[127]. Saaid et al. [61] utilized molding techniques to fabricate a transparent left ventricle (LV) to analyze interventricular fluid mechanics. To manufacture the phantom,

four layers of silicone were painted (brushed) onto a 3D printed LV mold. The model geometry was based on the statistical mean of a dataset of segmented 3D computed tomography images of 150 patients. Using a similar technique, Patel et al. [121], [128] manufactured bioengineered trileaflet valve (BETV) molds based on the geometry of a human infant aortic trileaflet valve. The molds were constructed using CAD software and computer numerical code (CNC) machining. As a limitation of CNC manufacturing, Patel et al. [121] reported that the CNC mold demonstrated significant variability compared to the CAD model. For example, the CNC mold was 8% smaller in height compared to the CAD model. Additionally, Narata et al. [109] used molding techniques in clinical research by manufacturing a physiological vessel using a positive hollow mold and casing. The casing was 3D printed from acrylic compound with constant offsets and inlets for injecting compliant material. The offsets between the positive mold and casing were chosen based on the mechanical requirements of the model (such as appropriate robustness), and to minimize ultrasound attenuations when analyzing the model. After removing any artifact left by the 3D printer, silicone was injected into the space between the positive mold and the casing. To facilitate the mold removal, a silicone oil layer (as a sealer) was applied to the interior surface of the casing prior to the silicone injection. The whole mold and casing system were placed inside a vacuum chamber to prevent wave scattering by bubbles when performing ultrasound measurements [109].

Based on the processes described by Trawiński et al. [119], molding techniques require precise temperature control through each time-consuming step. For example, to construct

their model of the left ventricle, Trawiński et al placed their mold in a freezer at  $-25 \pm 0.5$  °C for 35 hours, then allowed the model to thaw to room temperature for approximately 40 hours. Overall, the accuracy required within each step in the molding process reduces the efficiency and the applicability of this manufacturing technique in clinical research.

#### 2.4.2 Direct 3D printing

As an alternative, direct 3D printing offers a viable alternative manufacturing technique for cardiovascular models. More details can be found in several review papers on 3D printing applications in cardiovascular studies and surgical planning [129]–[134]. The most common 3D printing technologies that are applicable in cardiovascular research are: (1) Fused Deposition Modeling (FDM), (2) Selective Laser Sintering (SLS), (3) Stereolithography (SLA), (4) Color Inkjet Printing (CJP), and (5) Material Jetting (MJ) (Polyjet) [135]–[138]. These methods have enabled the simulation of a variety of diseases (such as aortic stenosis or calcified structures) using 3D models. Within this section, we will briefly discuss each of the above technologies, and their clinical applications.

Choosing a proper 3D printing technology relies on several factors including cost, precision, supporting material, transparency, speed, and post processing. Researchers must consider the benefits and limitations of various 3D printing methods based on their specific model and study requirements [69]. FDM involves melting a polymer through a nozzle and forming the desired geometry through material extrusion onto a flat substrate [139]. Despite being the most common 3D printing technology used today [135], FDM presents many

limitations as it requires support materials to prevent the model from collapsing during printing [140]. After printing, the supports can be removed mechanically (using a tool such as flush cutters or a water jet), or chemically (by dissolving the material in solution) [141]. The need for supporting material often prevents the printing of complex geometries and may influence the accuracy of the model, however, 3D printing via SLS (a subset of powder bed fusion 3D printing), does not require the use of supporting materials. To manufacture a phantom using SLS, a powder material is heated by a CO<sub>2</sub> laser to solidify the model layer by layer into the desired geometry [139]. In this case, easy removeable powders are attached to the surface which can be removed with a soft brush or pressurized air flow [142], [143]. Several powdered thermoplastic materials can be utilized when using a CO<sub>2</sub> laser, as CO<sub>2</sub> provides a higher power at lower cost [144]. Alternatively, SLA uses UV or visible light to polymerize a thin layer of a solution containing a photocrosslinkable resin. SLA allows for the 3D printing of transparent models with an ideal accuracy thus enabling optical diagnostics [139], however, SLA suffers from considerable cost and a need for supporting materials [142]. Photopolymer inkjet printing is a powder-based technology like SLS [145], which introduces a support-free color printing technology capable of generating complex geometries without the need for supporting material [146]–[148]. The head of the printer selectively sprays the color binder on the material (like how ink is deposited on paper) based on the printer settings, enabling researchers to distinguish between different organs and tissues [142]. Lastly, MJ allows for the combination of different materials within the 3D print, which can better represent the varied tissues within the heart wall [138].

To construct a model using MJ, fine drops of photopolymer are jetted onto the construction bed to attain the desired geometry and additional post-curing processes are not required after fabrication [142]. The resolution of this relatively accurate technique is highly dependent on the resolution of the inkjet printing head, the physical properties of the droplets, and the curing kinetics of the photopolymer. The minimum thickness and the minimum hole diameter of the model must be considered when using MJ for 3D printing. If the above specifications are not considered, MJ requires support for printing, which are jetted like the desired part [149].

Overall, direct 3D printing overcomes many of the constraints associated with molding, however, each 3D printing method introduces its own limitations which must be considered when selecting a technique for a cardiovascular study [142]. For example, Grab et al. [102] used Polyjet printing technology to establish a method for generating high-fidelity phantoms. The proposed workflow facilitated the creation of individualized models, enabling pre-interventional surgical planning and physician training on realistic anatomies. Polyjet printing allowed for the use of materials with different mechanical properties, resulting in phantoms with specific details of a disease and therefore better accuracy. Similarly, Maragiannis et al. [150] used fused dual-material 3D printing technology to model several aortic valve stenoses. The cusp calcifications were replicated using a rigid material, while the non-calcified structures (outflow tract, aortic root, and non-calcified valve cusps) were replicated using compliant materials. Again, the manufacturing technique chosen for this study allowed for the development of models with variable

material properties, improving fidelity. In addition to manufacturing phantoms based on imaging, 3D printing enables the customization of models to improve their accuracy. Vignali and colleagues [127] modified the geometry of an LV model to reproduce its dynamic properties, such as rotation, compression, and expansion. Proper replication of these properties required detailed manufacturing, achieved through Polyjet 3D printing technology. The accuracy provided by 3D models allows for a comprehensive understanding of anatomical features, assisting potential surgical interventions [130]. Furthermore, 3D printing can be used to manufacture custom-made clinical devices and implants, applicable in personalized patient care [138], [151]. The above studies have proven the ability of 3D printing technology to replicate appropriate anatomical and behavioral properties.

On balance, weighing up the pros and cons of both molding and 3D printing techniques – while considering the contemporary potentials – the molding technique is more favorable. Molding offers a wider range of material properties, which are long-wearing compared to 3D printed phantoms. As a result, it is more desirable to use the 3D printing to generate accurate molds and fabricate the phantom through molding via a proper rubber material. Moreover, modeling materials have superior optical features which facilitate visualization and optical measurements.

# Chapter 3

## 3 Experimental Methods

### 3.1 Methods

A mock flow circulation model was constructed which consisted of a left ventricle box, atrium tank, a piston pump, a realistic elastic silicone model of the left ventricle, a realistic aortic valve, a mechanical mitral valve, an adjustable systemic resistance, and a tunable compliance system (Figure 3.1). The elastic model of a left ventricle was fabricated through brushing multi-layers of silicone on an anatomically shaped mold reconstructed based on a data set obtained in an adult patient by computed tomography (CT) imaging. This technique applied successive layers of silicone on the mold until the left ventricle contraction and expansion and total left ventricular compliance match physiological values. The elastic model of the left ventricle used in this study has a shore hardness of 37A, which falls into the shore hardness range of the heart tissue. The aortic valve was also designed based on the realistic geometry from CT data, and the reconstructed geometry was manufactured through injection molding. Water was used as the working fluid on the circulatory side. A left ventricular pumping and compliance system containing distilled water was used to generate the physiological pulsating pumping action of the heart. The pump creates the left ventricle contraction and expansion. When the left ventricle model relaxes and initiates diastole during the expansion, the liquid is pumped into the left ventricle from the atrium tank and through the mitral valve. Once the contraction or systole phase begins, the liquid is pumped out

of the left ventricle, and after passing through the aortic valve, sent to the compliance chambers and systemic resistance. Finally, the flow exiting the systemic resistance returns to the atrium tank and closes the circulating system. The compliance and the resistance of the systemic arterial system can be adjusted to ensure physiological aortic pressure waveforms. Instantaneous flow rates were measured by two ultrasonic flow probes (Transonic, Ithaca, NY, USA) at the mitral valve inlet and aortic valve outlet [31], [85].

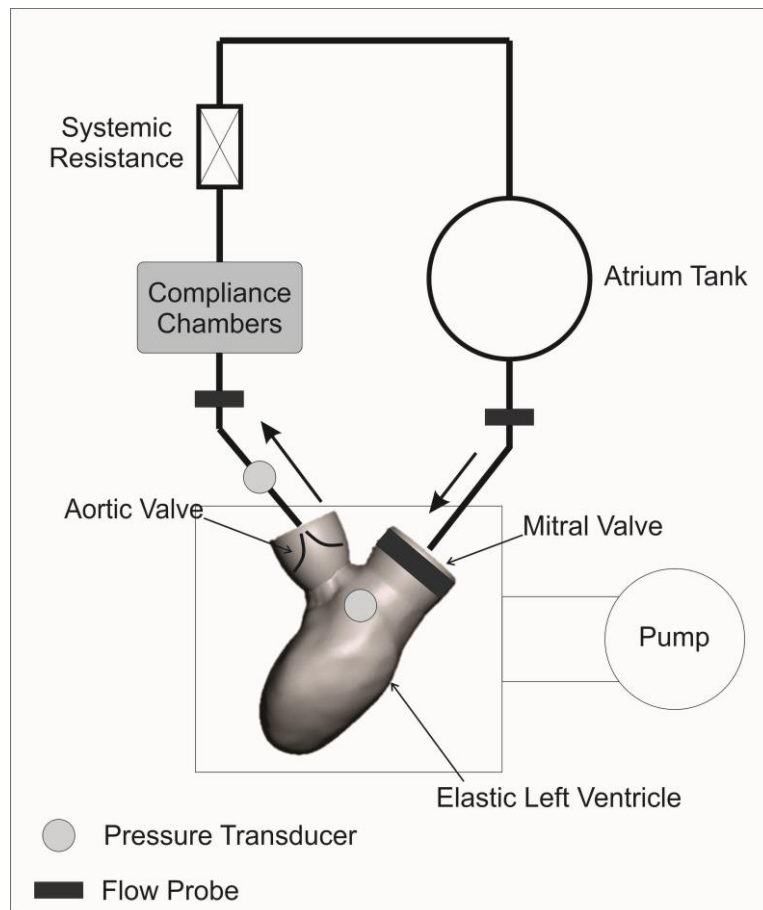


Figure 3.1 The schematic diagram of the cardiovascular simulator

The pressures in the left ventricle and aorta were measured using two fluid-filled pressure transducers (Blood Pressure Transducer; Utahmed, UT) located inside the left

ventricle and 5 cm upstream of the aortic valve, respectively. Pressure measurements determined the pressure variation during a cardiac cycle and pulse pressure. Both instantaneous flow rate and cardiac output were measured, and together with the pressure data, were used to calculate the systemic resistance and compliance for each case.

### 3.2 Experimental conditions

The simulator was tested in physiological conditions to simulate human systemic circulation. First, the left ventricle contraction and expansion were automatically dictated by a physiological waveform that is a function of time and imported to the pump controller via a software interface (ViViGen, ViVitro Labs, BC, Canada). This waveform specifies the left ventricle volume during diastole and systole; according to that the systole to diastole ratio is 40/60. The experimental test is started by turning on the tunable pump and gradually increasing the piston stroke amplitude. The system was tuned in four-stroke volumes of 30 ml, 40 ml, 50 ml, and 60 ml, while the heartbeat was kept at 70 bpm during the experiments. The systemic resistance and compliance were adjusted at each stroke volume to generate different physiological conditions and cardiovascular disorders. The left ventricle and mitral valve were kept unchanged, and four aortic valves with different thicknesses and stenotic conditions were tested. The pressure and flow were measured at each condition to study the system metrics.

The first aortic valve is used as a mild stenotic case and is a valve with a leaflet thickness of 0.3 mm and an aortic root size of 21 mm. A polyurethane rubber (VytaFlex™ 30, Smooth-on, Pennsylvania, US) with a shore hardness of 30 A was used to manufacture

the valve. In order to facilitate the valve installation into the simulator, the valve is equipped with a cylindrical scaffold with an inner diameter of 21 mm and an outer diameter of 25 mm. Similarly, three other valves with thicknesses of 0.6 mm, 0.8 mm, and 1 mm were manufactured and tested to simulate moderate to severe aortic stenosis.

The left ventricle was fabricated from a clear silicone with Shore 37A hardness (SORTA-Clear™ 37, Smooth-on, Pennsylvania, US). It comprises five layers of silicone brushed on a water-soluble material, and the average thickness of the left ventricle sac is 1 mm. A mechanical mitral valve is used to direct the flow to the left ventricle and prevent any back flows from the left ventricle to the atrium. In order to tune the left ventricle compliance and adjust its response to the pressure changes, the air content of the left ventricle box was controlled until reaching the left ventricle pressure trends resemble the physiological condition. In fact, the air content of the left ventricle box was used as viscoelastic impedance adapter to tune the left ventricle compliance, which led to a left ventricle stroke volume deviation from the pump stroke volume. A portion of the piston displacement was used to compress or expand the air volume of the viscoelastic impedance adapter. For correction, the piston amplitude was increased until reaching the cardiac output corresponding to the desired stroke volume to correct this difference. The flowmeter read the cardiac output and considering the heartbeat (70 beats/min), the stroke volume of the left ventricle was calculated.

Different systemic resistance conditions were manually created by changing the cross-sectional area of the tunable resistance. The change in the number and size of the compliance chambers and water/air ratio inside the compliance chambers led to changes

in compliance. Pressure values were recorded in each case, and using the stated equations in chapter 2, systemic resistance and compliance amounts were calculated.

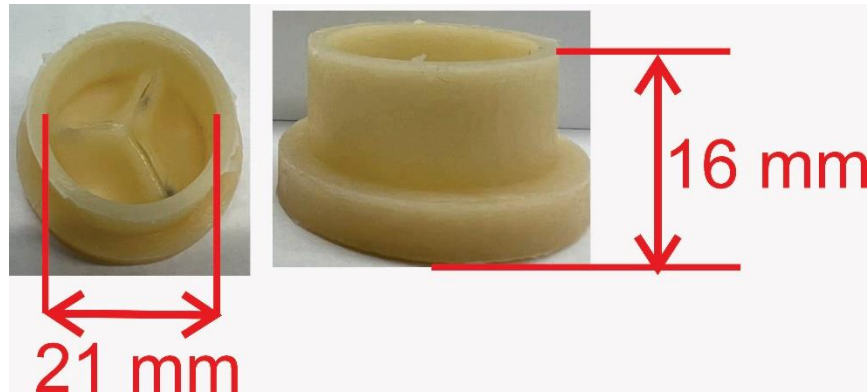
# Chapter 4

## 4 Results and Analysis

### 4.1 Aortic Valves

Aortic stenosis (AS), a narrowing of the aortic valve, is one of the most common and most serious valve problems. AS is a progressive disease in which the valve leaflets are thickened gradually. This is critical as such stenotic valves do not open appropriately.

In this work, we used a cardiovascular simulator to investigate the impact of hemodynamic parameters on the aortic stenosis function. Four aortic valves with the same physiological geometry (Figure 4.1) were fabricated with polyurethane materials, a material widely used in the medical industry [153]. The aortic valves and a silicone left ventricle were installed and tested in the cardiovascular simulator. The valve geometry was developed based on CT imaging data and extruded to four different thicknesses of 0.3 mm, 0.6 mm, 0.8 mm, and 1.0 mm. After geometry reconstruction, the valves were manufactured through injection molding. These stenotic valves were tested in the in vitro simulator under physiological conditions, and the impact of the systemic vascular resistance, stroke volume, and valve thickness on the hemodynamic parameters is presented in the results section below.



Valve Number	Valve #1	Valve #2	Valve #3	Valve #4
Leaflet Thickness	0.3 mm	0.6 mm	0.8 mm	1.0 mm

Figure 4.1 Fabricated valve dimensions: four valves of varying thicknesses manufactured through injection molding technique. The valve root diameter is 21 mm, and the valve holder cylinder has a height of 16 mm.

## 4.2 Systemic Vascular Resistance

A patient with a stenotic aortic valve often suffers from concomitant arterial diseases. This brings the left ventricle under a double load condition which is a combination of valvular load of AS and arterial load of vascular occlusion [153]. Arterial load can be quantified by SVR, which technically is a function of the blood vessel constriction and dilation, and when the vessel constricts, vasoconstriction occurs, and SVR increases. Conversely, vessel dilation or vasodilation results in a decrease in SVR. The amount of SVR varies from patient to patient and plays a vital role in cardiac pumping performance. In this section, to study the impact of the SVR variations on AS, valve #1 was tested in different vascular resistances by adjusting the peripheral resistance opening area (the cross-section of flow path). The peripheral resistance is a device with

adjustable porosity that can be changed to alter the resistance in the fluid flow. SVR can be calculated as a ratio of mean aortic pressure (MAP) [154] to the cardiac output (CO) [54], [154]:

$$SVR = \frac{MAP}{CO} \quad 4-1$$

Accordingly, the SVR was adjusted in this experiment by changing the flow cross-section in the peripheral resistance to mimic artery occlusions with different SVR ranges, and the stroke volume was kept in a constant amount of 50 ml.

#### 4.2.1 The Impact of SVR on the Left Ventricle and Aorta Pressures

The left ventricle and aorta pressures were measured in different SVRs and presented in Figure 4.2 and Figure 4.3. As highlighted in these figures, in response to the higher pressure-loss in the system, the left ventricle and aorta pressures increase. From a fluid mechanic perspective, the left ventricle, as a positive displacement pump, needs to increase the pressure to keep a constant flow rate and compensate for the pressure loss in the system. This puts higher stress on the left ventricle wall and increases the pressure on the fluid to overcome the elevated systemic resistance and deliver the required flow [155]. In this experiment, both left ventricle and aorta pressures show a linear variation with the SVR, where the left ventricle pressure rises with a slightly sharper slope.

Quantitatively, with a 49% increase in SVR, left ventricle and aorta peak pressures increase by 49% and 44%, respectively.

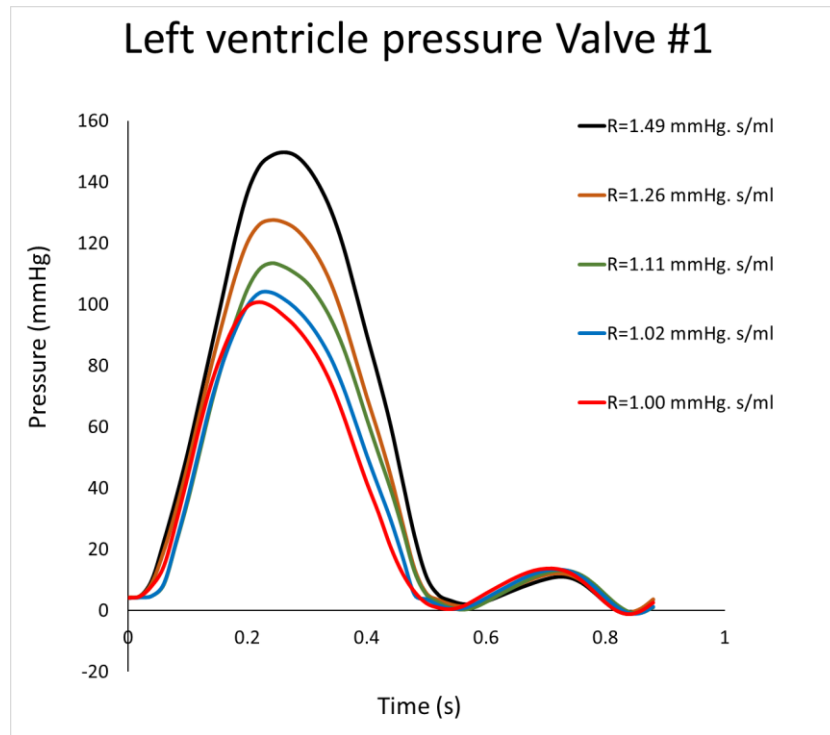


Figure 4.2 Variation of the left ventricular pressure with a gradual increase in systemic vascular resistance for valve #1 in stroke volume of 50 ml. In this test, valve #1 was used, and the systemic vascular resistance was changed using the adjustable resistance component in the cardiovascular simulator.

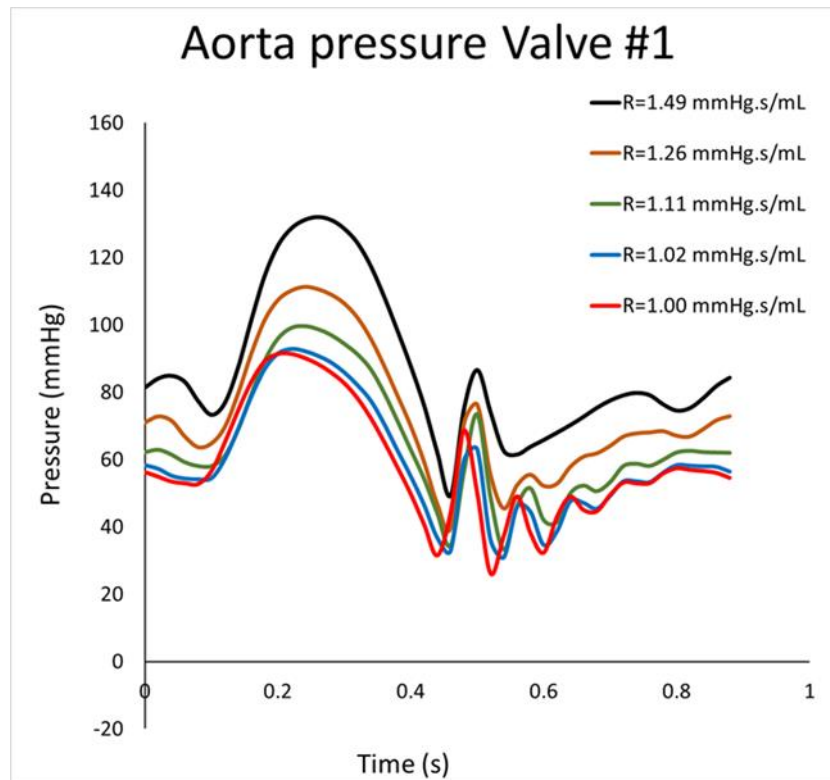


Figure 4.3 Variation of the aorta pressure with a gradual increase in systemic vascular resistance for valve #1 in stroke volume of 50 ml. In this test, valve #1 was used, and the systemic vascular resistance was changed using the adjustable resistance component in the cardiovascular simulator.

Peak to peak pressure gradient (PtoP PG) (Figure 4.4) is a parameter used to demonstrate the impact of SVR on the left ventricle and aortic valve performance. This experiment exemplifies hypertension patients with aortic stenosis, who experience elevated ventricular afterload due to valve lesions and heightened systemic vascular resistance [155]. Figure 4.5 shows how artery constriction condition can affect transvalvular pressure gradient. It can be noticed that for a valve with low stenotic severity, PtoP PG is significantly increased when the vascular occlusion increases, and this especially is more significant at lower SVRs. The pressure gradient is a measure to

classify different aortic stenosis categories and determine their severity. When comparing the pressure gradients of a single valve in different artery constrictions, with an increase in systemic resistance, the pressure gradient rises to more severe stenotic conditions. As it is shown in Figure 4.5, Valve #1 in a SVR of 1.00 mmHg.s/ml has a pressure gradient of 9.4 mmHg, which falls in the range of mild aortic stenosis. The increase in SVR intensifies the severity of aortic stenosis and in SVR of 1.49 mmHg.s/ml, a shift from mild to moderate aortic stenosis happens, and the intervalvular pressure gradient becomes 17.6 mmHg. As it is mentioned before, the increases in pressure gradient with SVR is more notable in lower SVRs. For example, for a 11% increase in SVR from 1.00 mmHg.s/ml to 1.11 mmHg.s/ml, the pressure gradient increases substantially by 48% from 9.4 mmHg to 13.9 mmHg. However, in higher SVR quantities, with a 35% rise in SVR from 1.11 mmHg.s/ml to 1.49 mmHg.s/ml, the pressure gradient has a comparatively lower increase of 27%.

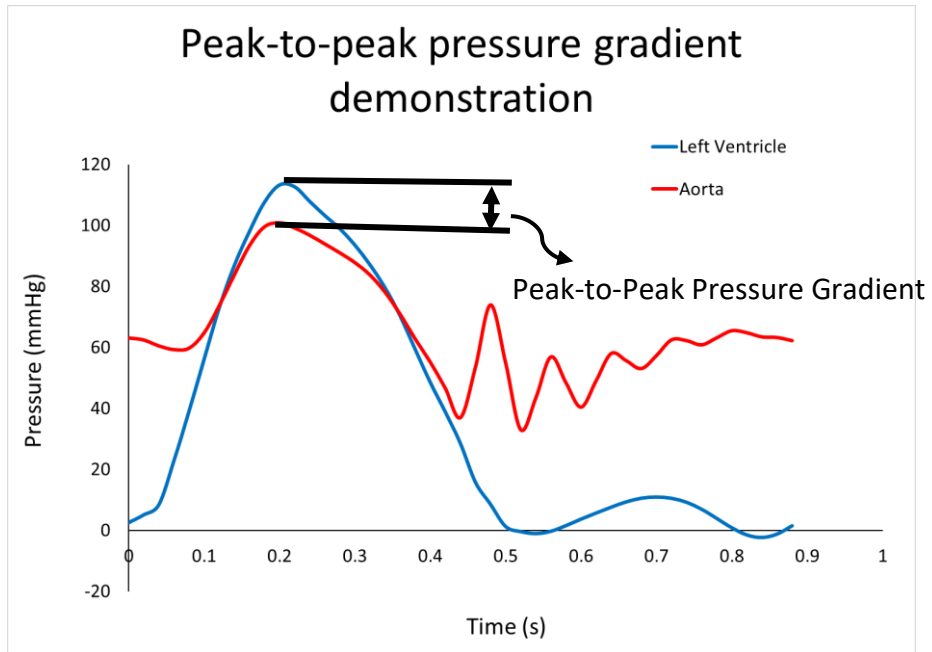


Figure 4.4 A demonstration of the peak-to-peak pressure gradient on the left ventricle and aorta pressure waveforms

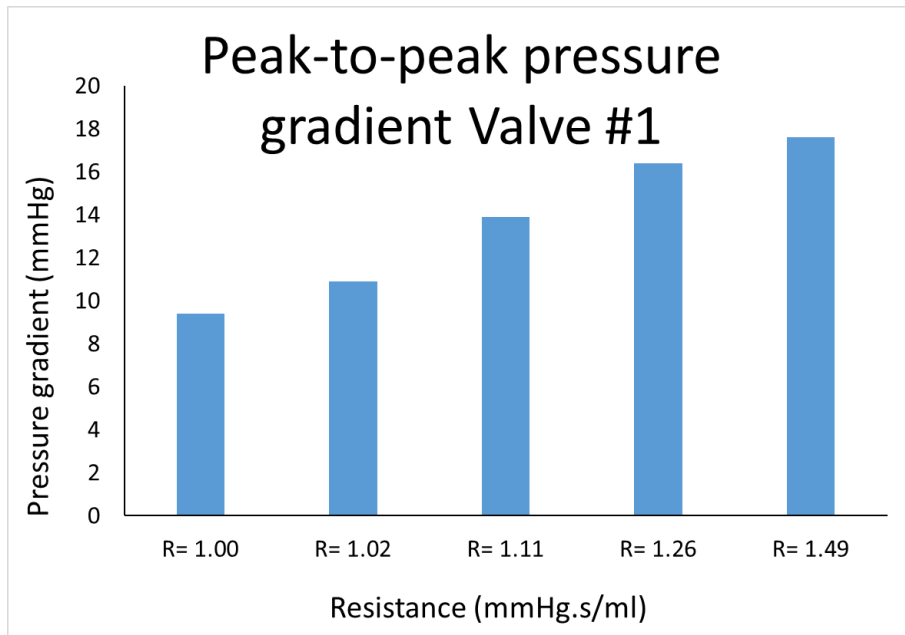


Figure 4.5 The impact of systemic vascular resistance on the peak-to-peak pressure gradient of Valve #1 in a stroke volume of 50 ml.

#### 4.2.2 The Impact of SVR on the Effective Orifice Area

Effective orifice area (EOA) is a measure of the aortic valve opening area and is calculated based on equation 4-2. To calculate the EOA for valve #1 in different conditions, parameters were chosen based on the ISO5840-3 standard [156], and the EOA (cm<sup>2</sup>) was derived as:

$$EOA = \frac{q_V}{51.6 \sqrt{\frac{\Delta P}{\rho}}} \quad 4-2$$

Where  $q_V$  is the forward volumetric flow (ml/s),  $\Delta P$  (mmHg) is the mean pressure difference during systole, and  $\rho$  (g/cm<sup>3</sup>) is the working fluid density. Using the measured data for Valve #1 at different SVRs, EOAs are calculated and shown in Figure 4.6. Since EOA is a function of the square root of the mean pressure gradient, it is highly dependent on upstream conditions such as SVR values. As illustrated in Figure 4.6, with an increase in the SVR, the effective orifice area becomes smaller. Results from the in vitro measurements demonstrate that EOA is greatly affected by the variation of the SVR. An elevated SVR causes a higher back-pressure on the valve leaflets and makes it difficult for the valve to open properly, which reduces the valve opening or EOA. For all artery constriction severities, EOA decreases significantly, when SVR was increased from 1.00 to 1.49 mmHg.s/ml. As a quantitative example, the EOA for valve #1 at SVR= 1.00 mmHg.s/ml is equal to 0.37 cm<sup>2</sup>, and with a 49% rise in SVR from 1.00 to 1.49 mmHg.s/ml, the EOA drops by almost 27% from 0.37 cm<sup>2</sup> to 0.25 cm<sup>2</sup>. It is observed that EOA is more susceptible to SVR changes at lower SVR values. In lower SVRs, the EOA changes more severely and an 11% increase in SVR from 1.00

mmHg.s/ml to 1.11 mmHg.s/ml leads to an 18% decrease EOA. However, the EOA variation rate declines in higher SVRs, where there is less significant change in EOA due to SVR changes. For instance, a 35% rise in SVR from 1.11 mmHg.s/ml to 1.49 mmHg.s/ml results in an only 11% reduction in EOA.

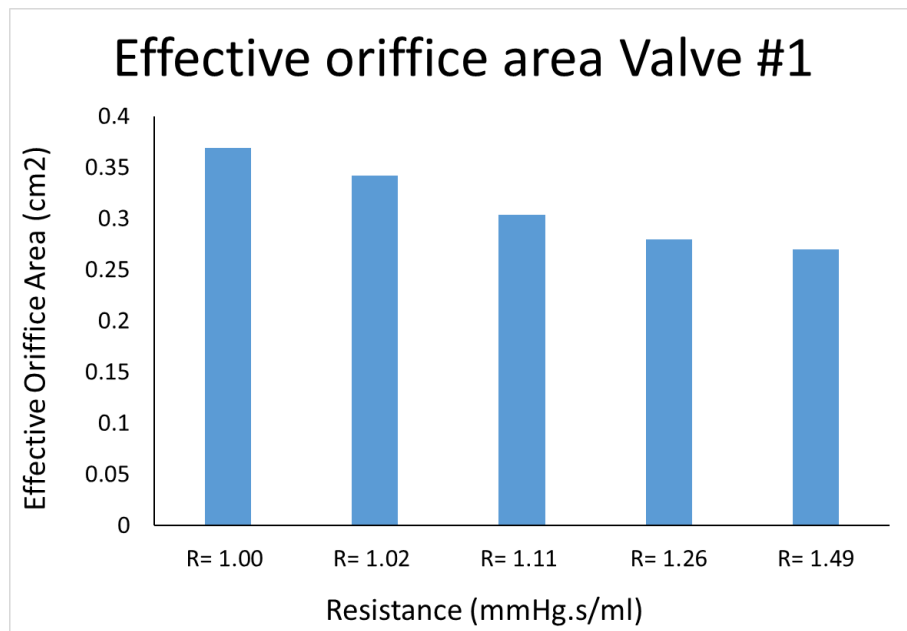


Figure 4.6 The impact of systemic vascular resistance on the Effective Orifice Area (EOA) of Valve #1 in a stroke volume of 50 ml.

#### 4.2.3 The Impact of SVR on the Left Ventricle Workload

An alternative approach to describe heart diseases severity, such as aortic stenosis and artery constriction, is the total workload that the left ventricle uses to open the aortic valve and deliver the blood flow to the body, and it is calculated as the integral of the left ventricle pressure times its volume [157], [158]:

$$W = \int PdV \quad 4-3$$

The pressure that the left ventricle needs to overcome during each contraction is called afterload and in circumstances like hypertension, the left ventricle must work harder to overcome the elevated afterload [158]–[170]. In chronic intensified afterload conditions, the left ventricle undergoes hypertrophy which is the thickening of left ventricle muscles. As it is shown in Figure 4.7, left ventricle workload increases with SVR and this increase is especially notable in the higher SVRs. According to Figure 4.7, for a 49% increase in SVR from 1.00 mmHg.s/ml to 1.49 mmHg.s/ml, the LV workload increases by 79% from 0.6 J to 1.1 J.

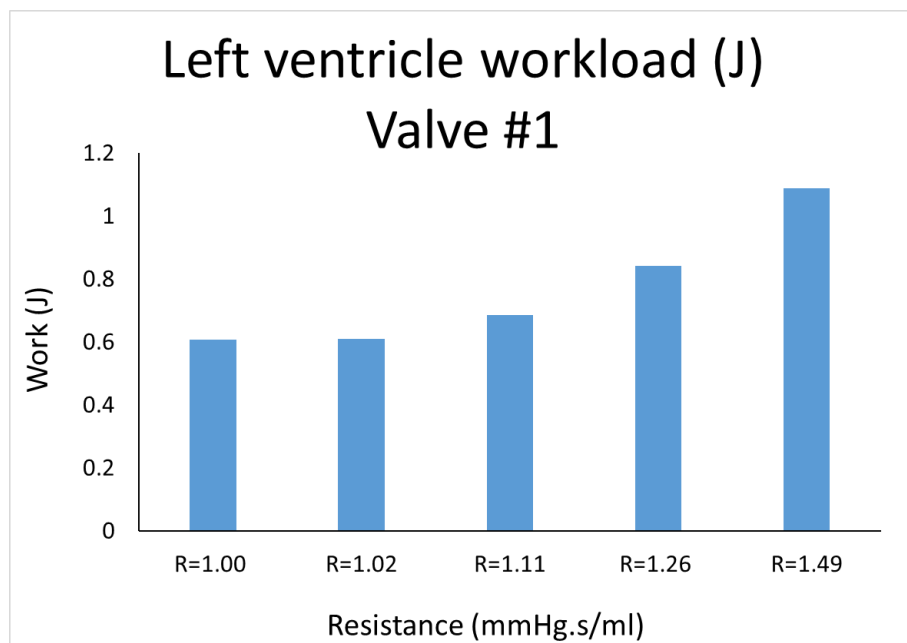


Figure 4.7 The impact of systemic vascular resistance on the left ventricle workload of Valve #1 in a stroke volume of 50 ml. The left ventricle workload can be computed as

$$W = \int P dV$$

where  $P$  is the instantaneous left ventricle pressure and  $V$  is the corresponding volume.

## 4.3 Stroke Volume

This section investigates the impact of stroke volume as one of the most critical parameters in blood flow hemodynamics. Valve #1 with a leaflet thickness of 0.3 mm was installed in the cardiovascular simulator, and the stroke volume was increased gradually from 30 ml to 60 ml. During the test, peripheral resistance and compliance of the circulatory system were kept unchanged at all stroke volumes. The pressure and flow were measured, and the results are presented here.

### 4.3.1 The Impact of the Stroke Volume on the Left Ventricle and Aorta Pressure

A change or modification in the stroke volume is attributed to changes in ventricular contractility [158] in which a rise in the duration and amount of contraction generates a higher stroke volume [171]. To simulate this physiological phenomenon, the stroke volume increased, and the results of the left ventricle and aorta pressures were measured and presented in Figure 4.8 and Figure 4.9. Figures 4.8 and 4.9 show that with an increase in the left ventricle contraction during systole, the left ventricle wall withstands a higher stress level, and this leads to a linear increase in the left ventricle and aorta pressures. According to the in vitro results, with an 100% increase in stroke volume (30-60ml), the left ventricle and aorta peak pressures increase by 106% and 108%, respectively. During the diastole (Figure 4.8), with a drop in the stroke volume, the left ventricle filling pressure increases, representing a diastolic dysfunction that generally happens when the left ventricle walls become stiffer [171]. In order to assess the effects

of stroke volume on the left ventricle and aorta pressures simultaneously, the intervalvular aortic valve pressure gradient is calculated and compared in Figure 4.10. Accordingly, the pressure gradient increases with an increase in stroke volume. This trend can be explained by the aortic valve resistance concept. Considering a unique valve with constant anatomical resistance, the pressure gradient is a function of flow rate across the valve [172], [173]. As a result, with an increase in the flow rate or stroke volume, the transvalvular pressure gradient rises.

$$\Delta P \propto R \times SV^n \qquad 4-4$$

Where  $\Delta P$  is the transvalvular pressure gradient,  $R$  is the aortic valve resistance,  $SV$  is the stroke volume, and  $n$  is a constant. Based on the measured data in the experiment,  $n \approx 1$  and the pressure gradient across the aortic valve in this range of stroke volume varies linearly with the flow rate. Quantitatively, with an 100% increase in stroke volume (30-60ml), PtoP pressure gradient increases by 91.4% (7.4-14.2 mmHg).

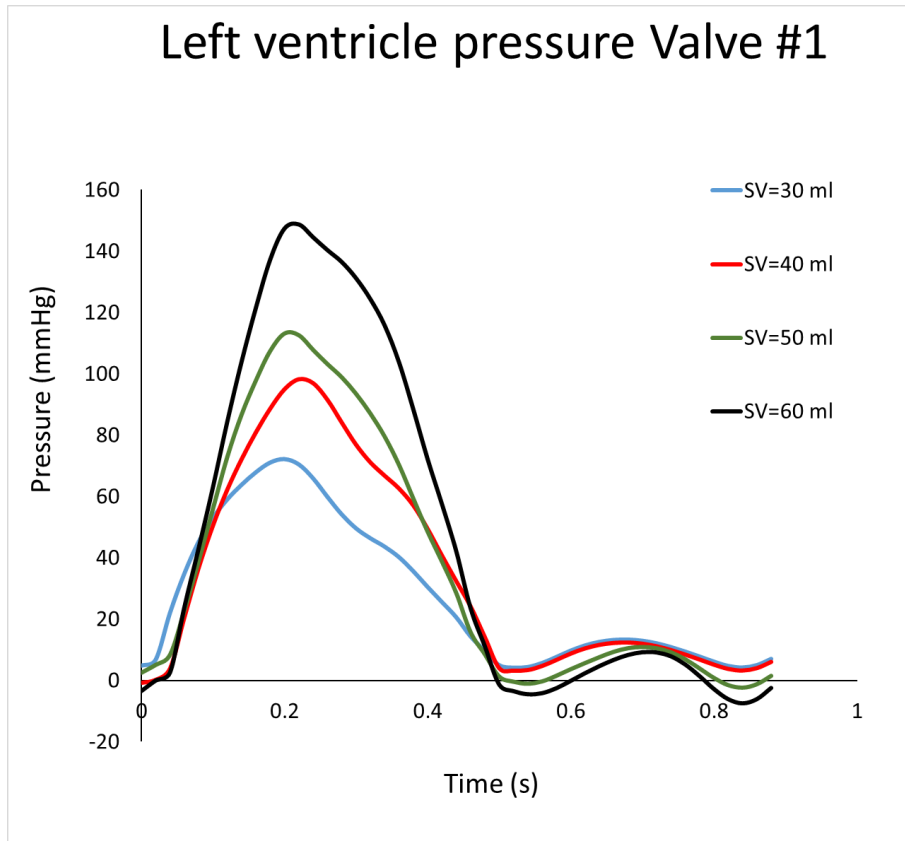


Figure 4.8 Variation of the left ventricular pressure with stroke volume for valve #1. Peripheral resistance and systemic compliance were kept unchanged during the experiments.

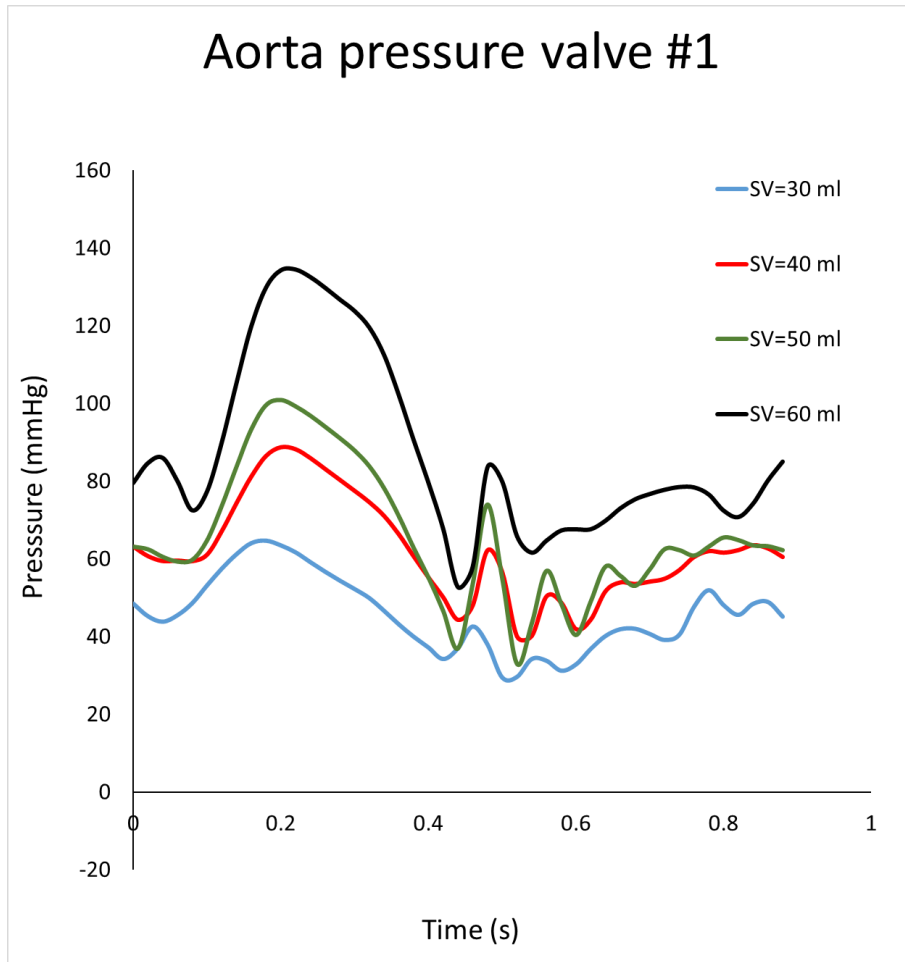


Figure 4.9 Variation of the aorta pressure with varying the stroke volumes for valve #1. Peripheral resistance and systemic compliance were kept unchanged during the experiments.

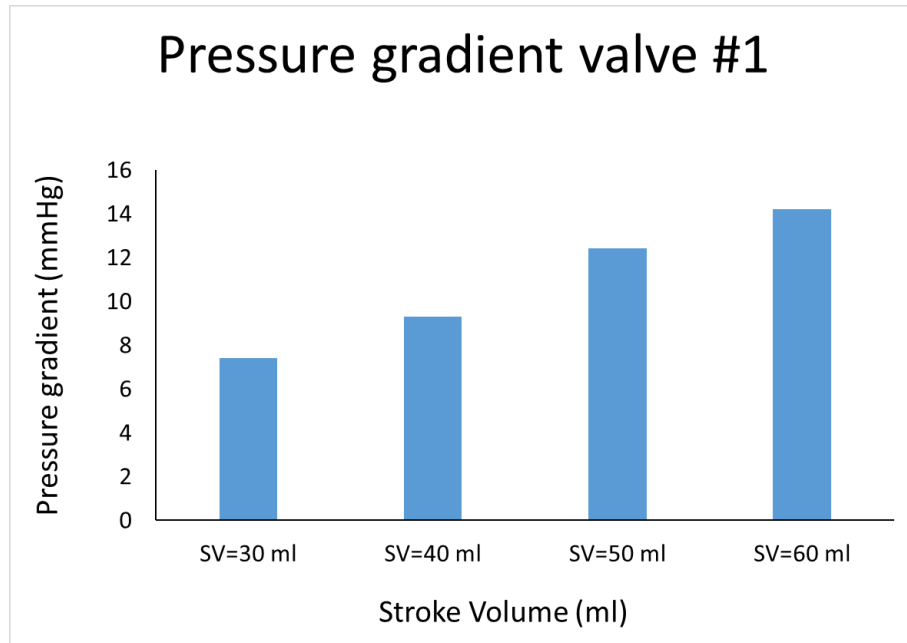


Figure 4.10 The impact of the stroke volume on the transvalvular peak- to-peak pressure gradient for Valve #1. The simulator was tested with stroke volumes of 30 ml, 40 ml, 50 ml, and 60 ml. Peripheral resistance and systemic compliance were kept unchanged during the experiments.

#### 4.3.2 The Impact of the Stroke Volume on the Effective Orifice Area

The dependence of the valve opening area on the stroke volume, particularly in low cardiac outputs of left ventricular dysfunction is of paramount importance. In valve #1 with mild stenosis, the left ventricle is not capable of providing enough flow and force to open the valve. This condition can lead to low EOA and is called *pseudo-severe* stenosis [174]. According to equation 4-2, EOA is directly proportional to the flow rate and inversely proportional to the square root of the mean pressure gradient. With an increase in stroke volume, both the flow rate and the pressure gradient rise, and their concomitant effects determine the trends of EOA. The in vitro measurements show that the effect of the stroke volume on the EOA is the inverse of that of the SVR: increase

in the stroke volume increases the EOA (Figure 4.11). As illustrated in Figure 4.11, without any anatomical change in the simulator, EOA increases with the flow rate linearly, which are in agreements with other studies [174], [175]. In this experiment, EOA increased by 44.5% ( $0.25\text{--}0.36\text{ cm}^2$ ) with an 100% increase in stroke volume (30–60 ml). Although, the EOA is inversely proportional to the square root of the mean pressure gradient, both intervalvular pressure gradient and EOA increase with the increase in stroke volume. At stroke volume of 30 ml, the pressure gradient and EOA are 7.4 mmHg and  $0.25\text{ cm}^2$ , respectively. On the other hand, at stroke volume of 60 ml, the pressure gradient and EOA are 14.2 mmHg and  $0.36\text{ cm}^2$ , respectively. This shows that, despite the lower amount of pressure gradient in stroke volume of 30 ml, the valve has a smaller effective orifice area; hence, experiences a more severe aortic stenosis.

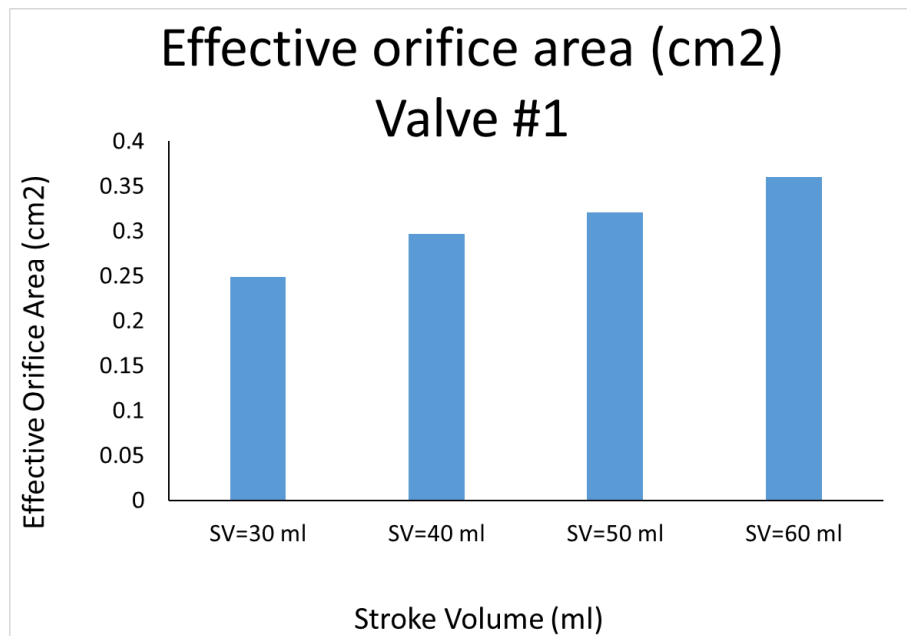


Figure 4.11 The impact of the stroke volume on the effective orifice area ( $\text{cm}^2$ ) for Valve #1. The simulator was tested with stroke volume of 30 ml, 40 ml, 50 ml, and 60

ml. Peripheral resistance and systemic compliance were kept unchanged during the experiments.

## 4.4 Aortic Valve Thickness

Aortic valve diseases range from mild leaflet thickening to severe aortic stenosis [176]. Aortic stenosis is a progressive disease in which the leaflets thicken gradually. To investigate the impact of leaflet thickening on valve hemodynamics, four aortic valves with the same geometry but different leaflet thicknesses (Figure 4.1) were designed and manufactured to simulate a range of aortic valve stenosis.

### 4.4.1 The Impact of the Leaflet Thickness on the Left Ventricle and Aorta Pressures

A thicker valve leads to a narrower aortic valve opening and left ventricle overload [177]. As a result, the left ventricle works harder to overcome the elevated aortic resistance and pump the required flow, which puts higher stress on the left ventricle walls and muscles. As outlined in Figure 4.12, this increase in the left ventricle wall stress leads to a higher left ventricle pressure as well. Aortic pressure also demonstrates an increase due to a left ventricle pressure rise (Figure 4.13); however, the rate of increase of left ventricle pressure is notably higher compared to the aortic pressure rise. For example, with an increase in thickness from 0.3 mm to 1 mm, the left ventricle peak pressure increases by 38.6% (from 113.2 mmHg to 156.9 mmHg). While for the same change in the thickness, the aorta peak pressure rises by 12.9 % (from 100.8 mmHg to 113.8 mmHg).

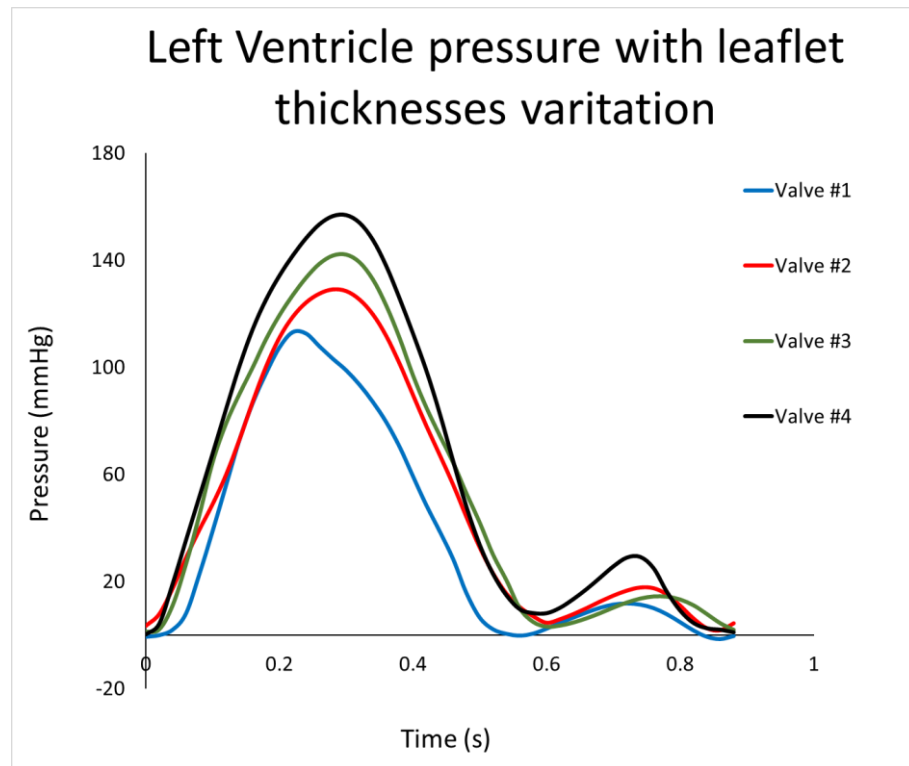


Figure 4.12 Variation of the left ventricle pressure with the change in leaflet thickness. Four valves with the same geometry and different leaflet thicknesses were tested in stroke volume of 50 ml. Peripheral resistance and systemic compliance were kept unchanged during the experiments.

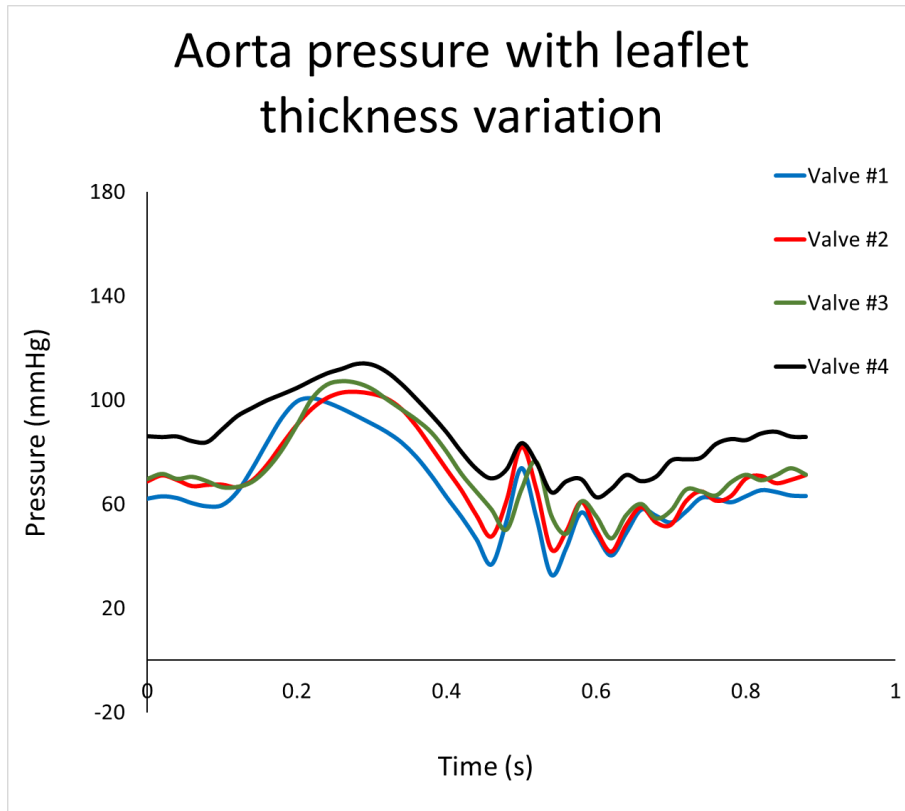


Figure 4.13 Variation of the aorta pressure with changes in leaflet thickness. Four valves with the same geometry and different leaflet thicknesses were tested in stroke volume of 50 ml. Peripheral resistance and systemic compliance were kept unchanged during the experiments.

The difference in the rate of left ventricle and aorta pressure rises that outlined here testifies to the fact that a higher leaflet thickness increases the valve resistance, and this is reflected in the pressure gradient rise. As described in equation 4-4, for a valve with higher resistance, the pressure gradient is higher (in a constant flowrate). As it is represented in Figure 4.14, valve #1 has a pressure gradient of 12.4 mmHg which falls in the mild aortic stenosis area. As thickness and aortic stenosis severity increases, the pressure gradient increases with the thickness linearly. For valve #2 and valve #3, the

pressure gradients are 25.9 mmHg and 34.9 mmHg, respectively, which are in the range of moderate to severe aortic stenosis. Finally, valve #4 demonstrates a pressure gradient of 43.1 mmHg, which replicates severe stenosis. Please note all four valves have the same geometry but different leaflet thicknesses, in which Valve #1 has the thinnest leaflets (0.3 mm) and valve #4 has the thickest leaflets (1.0 mm). Figure 4.15 to Figure 4.18 demonstrate left ventricle, aorta pressures and their peak-to-peak pressure gradient at the same time.

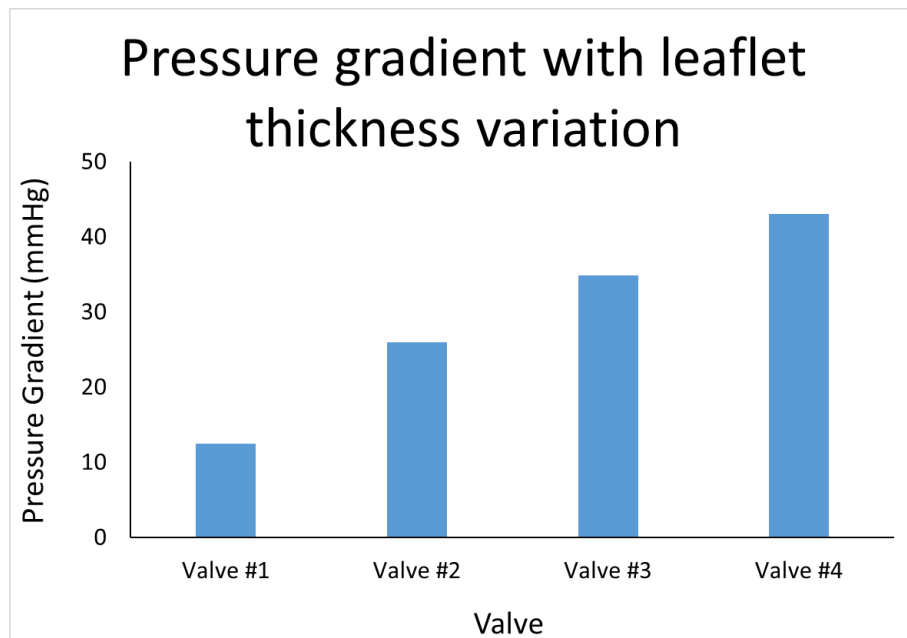


Figure 4.14 The leaflet thickness impact on the pressure gradient in the constant stroke volume of 50 ml.

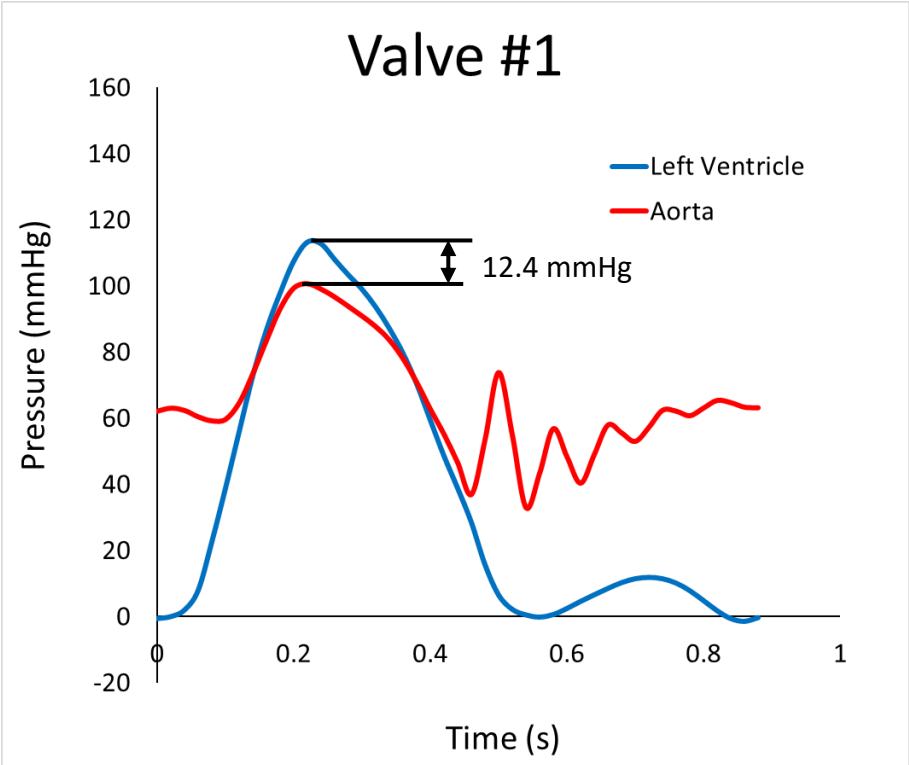


Figure 4.15 Left ventricle pressure, aorta pressure and the peak-to-peak pressure gradient for Valve #1 at stroke volume of 50 ml.

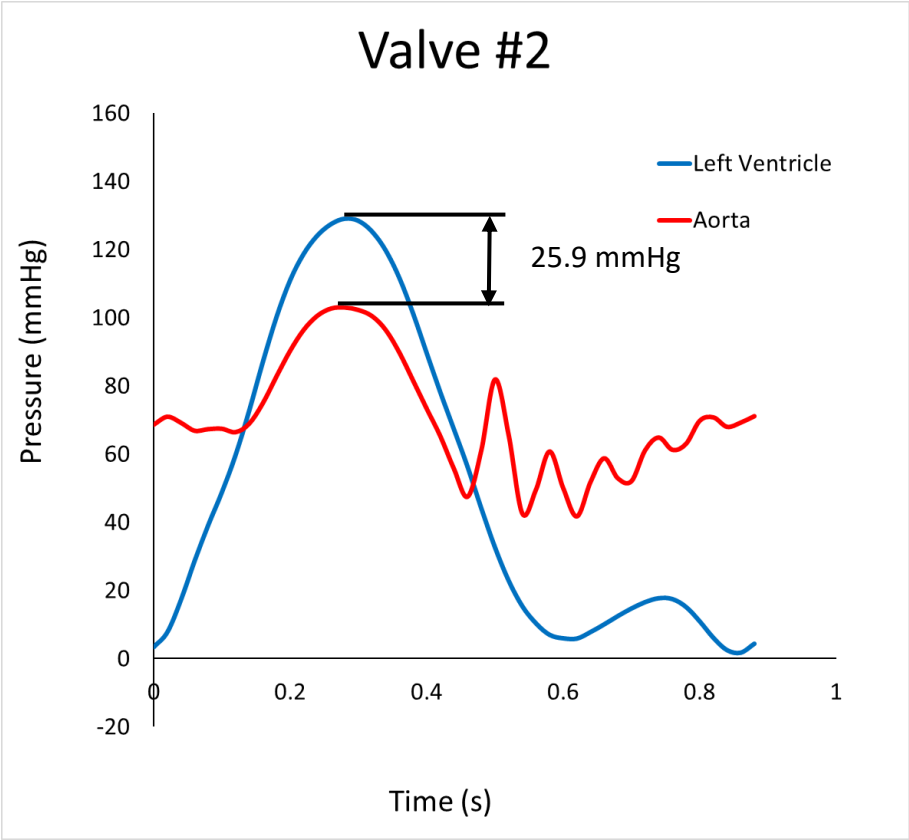


Figure 4.16 Left ventricle, aorta pressures and the peak-to-peak pressure gradient for Valve #2 at stroke volume of 50 ml.

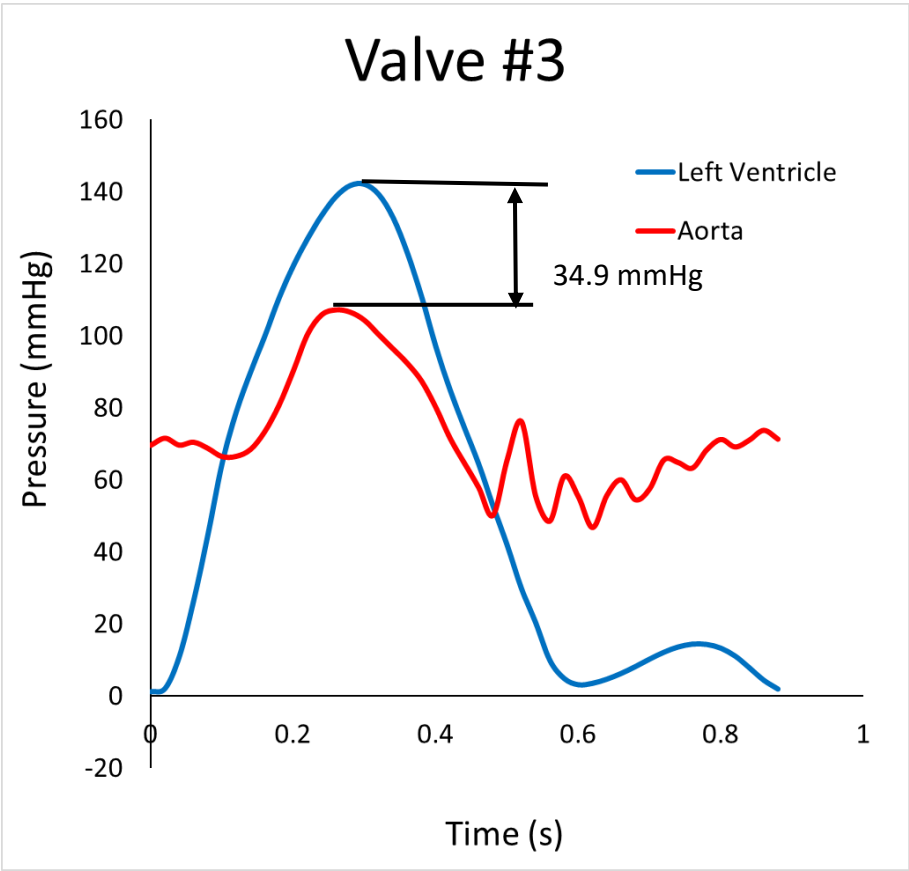


Figure 4.17 Left ventricle, aorta pressures and the peak-to-peak pressure gradient for Valve #3 at stroke volume of 50 ml.

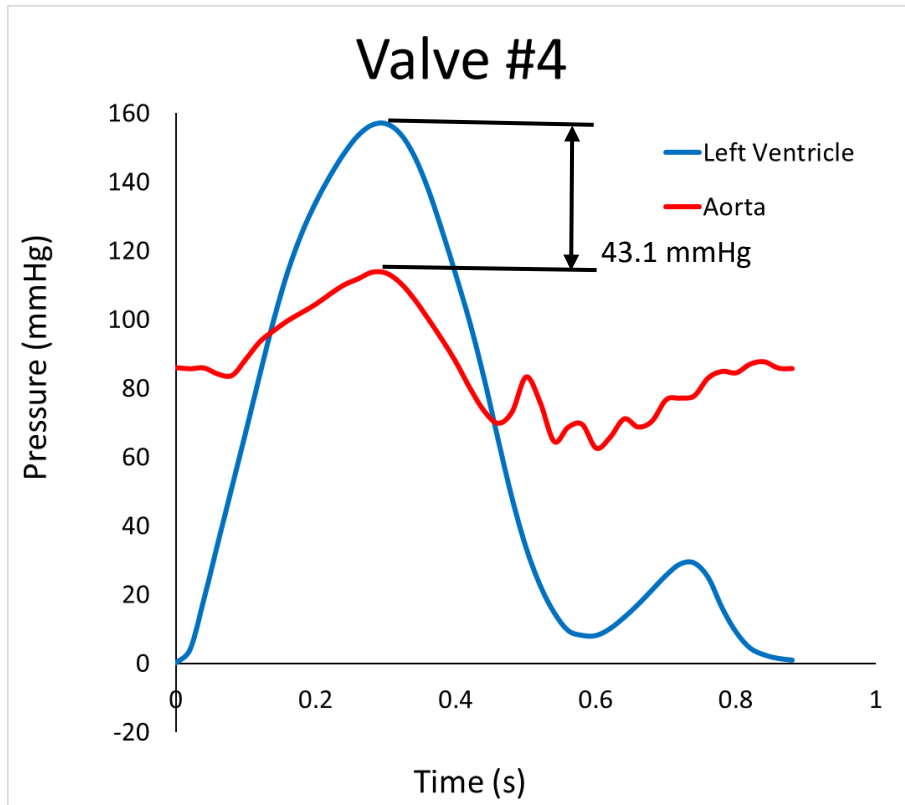


Figure 4.18 Left ventricle, aorta pressures and the peak-to-peak pressure gradient for Valve #4 at stroke volume of 50 ml.

#### 4.4.2 The Impact of the Leaflet Thickness on the Effective Orifice Area

As illustrated previously, the EOA is inversely proportional to the mean pressure gradient and can be used to quantify and classify aortic stenosis severity. A thicker valve leaflet leads to smaller effective orifice area. This can be explained through the concept of cantilever beams, which are used to describe the valve opening and leaflet deflection in the commissural region, where the leaflets join the aortic root [178]. According to the cantilever beam deflection correlation, the amount of deflection is Inversely proportional to the moment of inertia and thickness. As a result of leaflet thickening, the leaflet deflection and valve opening area at each forward stroke reduce. In vitro, as

described in Figure 4.19, the effective orifice area reduces with an increase in leaflet thickness, which is consistent with the cantilever beam analogy. The impact of leaflet thickness on EOA is more notable in thinner valves. For instance, a 0.2 mm thickness increment from 0.6 mm to 0.8 mm and from 0.8 mm to 1.0 mm leads to a 14% and 10% decrease in EOA, respectively. Furthermore, it appears that in higher thicknesses, the EOA approaches to constant values and there is a smaller change in EOA.

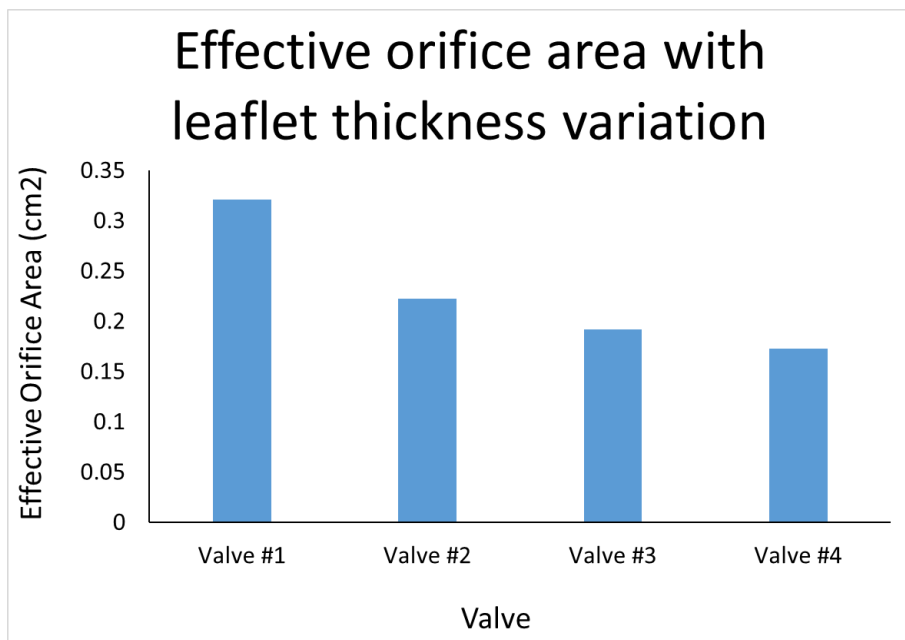


Figure 4.19 Effective orifice area variations with a change in the thickness of leaflet at stroke volume of 50 ml.

#### 4.4.3 The Impact of Thickness on the Left Ventricle Workload

Left ventricle workload is a representation of the LV energetic state and is a function of ventricular geometry, its mechanical properties, and valvular and vascular condition [179]. With an increase in aortic valve impedance, the left ventricle uses more energy to deliver constant blood flow rate to the body. As shown in

Figure 4.20, with leaflet thickness increment, LV stroke work changes slightly from 0.65 J for valve #1 to 0.67 J for valve #2 (a 3% increase). However, as the leaflets thicken, the LV workload worsens considerably [180]. Accordingly, for a thickness change from 0.8 mm in valve #3 to 1.0 mm in valve #4, the LV workload increases by 10%. In general, a change in leaflet thickness from 0.3 mm to 1.0 mm leads to a 34% increase in the LV workload. This is critical as by increasing the LV workload, the heart should pump harder to compensate for this increase which leads to heart failure.

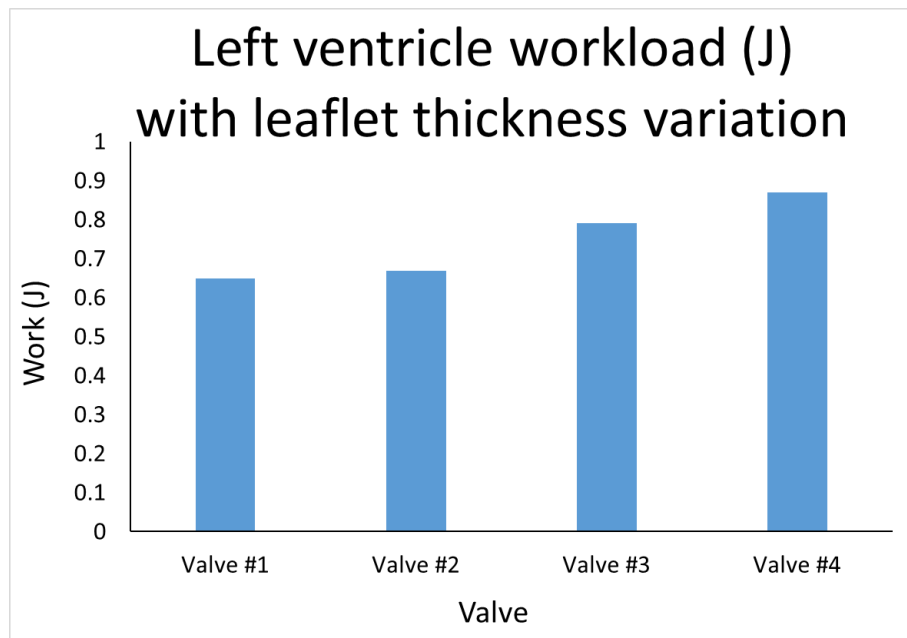


Figure 4.20 The variation in the left ventricle workload with the change in aortic valve thickness at stroke volume of 50 ml. The left ventricle workload is a function of the left ventricle pressure and volume, and it can be calculated by  $W_{LV} = \int P dV$  where P and V are LV volume and pressure, respectively.

# Chapter 5

## 5 Limitations and Conclusion

### 5.1 Limitations

In this experiment, water was used instead of blood due to the high volume of the required working fluid. The results that were claimed in this thesis were tested only one time. Therefore, we do not have any statistical or uncertainty analysis to demonstrate the findings of this study.

### 5.2 Conclusion

This experimental study was performed to assess the impact of different hemodynamic parameters on the severity of aortic stenosis. A stenotic aortic valve geometry was reconstructed using computed tomography images and manufactured through an injection molding technique. The valve installed and tested in a cardiovascular simulator under different hemodynamic conditions to investigate the impacts of systemic vascular resistance, stroke volume, and leaflet thickness on the aortic stenosis.

Patients with aortic stenosis often suffer from artery occlusion and vascular diseases. Consequently, the left ventricle comes under a double load condition, which is due to the concomitant occurrence of AS and artery constriction. In vitro results demonstrate that with an increase in SVR, the left ventricular load increases. A 49% increase in SVR results in a 49% and 44% rise in the left ventricle and aorta pressures, respectively. In a patient with aortic stenosis and hypertension, the peak-to-peak pressure gradient rises

with the SVR increase, which is particularly notable in lower SVRs. For an 11% change in SVR (1.00 to 1.11 mmHg.s/ml), the pressure gradient rises considerably by 48% (9.4 to 13.9 mmHg). While, in higher SVR values, when the artery becomes more constricted, a 35% rise in SVR (1.11 to 1.49 mmHg.s/ml) results in only a 27% increase in pressure gradient (13.9 to 17.6 mmHg). SVR change has a direct bearing on EOA and with a +49% SVR change, EOA varies by +27%. Ostensibly, the double load condition which stemmed from the concomitant rise of AS and artery disease, makes the left ventricle work harder to generate more pumping energy, especially in higher SVR values. The experimental results show a 79% LV workload increment for a 49% increase in SVR.

In addition to vascular diseases, ventricular insufficiency may impact the AS severity. The left ventricular insufficiency was modeled as the low stroke volume condition, which is a key factor in pseudo-severe stenosis occurrence. The experimental measurements portrayed a linear increase in both left ventricle and aorta peak pressures with the stroke volume increment. The peak-to-peak pressure gradient across the aortic valve is a function of the valve geometry and mechanical properties, as well as the flow conditions. In a specific valve, the PtoP PG increases linearly with an increase in flow rate. Furthermore, EOA increases with the stroke volume, which shows that the valve at a lower stroke volume suffers from a more severe AS. In vitro results demonstrate a linear change in EOA with the stroke volume, where a 100% increase in stroke volume (30-60 ml) results in a +44.5% rise in EOA (0.25–0.36 cm<sup>2</sup>).

Finally, the impact of the leaflet thickness on the AS was assessed. The aforementioned results suggest that both left ventricle and aorta pressure increase with leaflet

thickening; however, the rate of increase of left ventricle pressure is notably higher compared to the aortic pressure. An increase in thickness from 0.3 to 1.0 mm leads to 38.6% and 12.9% increases in the left ventricle and aorta peak pressures, respectively. The finding of this study shows that changing the leaflet thickness can be used to simulate different ranges of AS, in vitro. EOA is also intensely influenced by the leaflet thickness, which is particularly notable in lower thicknesses. A leaflet thickening from 0.3 mm to 1.0 mm results in a 46% reduction in EOA. The resulting valvular lesion leads to a higher left ventricle workload and energy consumption. According to our findings, with a change in leaflet thickness from 0.3 mm to 1.0 mm, the LV workload increases by 34%.

It is concluded that the aortic stenosis severity may be changed by changes in systemic vascular resistance, leaflets' thickness as well as flow conditions. Such impacts may increase the left ventricle workload, resulting to heart failure and left ventricle hypertrophy. We concluded that that the severity of aortic stenosis not only depends on the valve geometrical parameters but also can be influenced significantly by hemodynamics parameters.

## Bibliography

- [1] A.-E. M. Kerlo, “Experimental study of pathological and cardiovascular device hemodynamics,” PhD Thesis, Purdue University, 2013.
- [2] P. S. Mekala, “Comparative Study of Diastolic Filling under Varying Left Ventricular Wall Stiffness,” Jul. 2015, Accessed: Oct. 28, 2020. [Online]. Available: <https://shareok.org/handle/11244/45282>
- [3] B. D. Jones, *Comprehensive medical terminology*. Cengage Learning, 2015.
- [4] M. Abbasi, “Computational Modeling of Transcatheter Aortic Valves,” PhD Thesis, University of Denver, 2018.
- [5] P. A. Iaizzo, *Handbook of Cardiac Anatomy, Physiology, and Devices*. Springer Science & Business Media, 2010.
- [6] I. Lakshmi, “Chapter 3 - Anatomical photo representations for cardiac imaging training,” in *Image Processing for Automated Diagnosis of Cardiac Diseases*, K. Chauhan and R. K. Chauhan, Eds. Academic Press, 2021, pp. 35–48. doi: 10.1016/B978-0-323-85064-3.00005-4.
- [7] A. Ostadfar, “Chapter 4 - Biofluid Dynamics in Human Organs,” in *Biofluid Mechanics*, A. Ostadfar, Ed. Academic Press, 2016, pp. 111–204. doi: 10.1016/B978-0-12-802408-9.00004-1.
- [8] S. Whiteman, Y. Alimi, M. Carrasco, J. Gielecki, A. Zurada, and M. Loukas, “Anatomy of the cardiac chambers: A review of the left ventricle,” *Translational Research in Anatomy*, vol. 23, p. 100095, 2021.
- [9] K. B. Chandran, S. E. Rittgers, and A. P. Yoganathan, *Biofluid mechanics: the human circulation*. CRC press, 2006.
- [10] D. Oliveira, J. Srinivasan, D. Espino, K. Buchan, D. Dawson, and D. Shepherd, “Geometric description for the anatomy of the mitral valve: A review,” *Journal of Anatomy*, vol. 237, no. 2, pp. 209–224, 2020, doi: 10.1111/joa.13196.
- [11] “Heart valve disease - Symptoms and causes,” *Mayo Clinic*. <https://www.mayoclinic.org/diseases-conditions/heart-valve-disease/symptoms-causes/syc-20353727> (accessed Jun. 27, 2022).

- [12] Y. S. Morsi and Y. S. Morsi, *Tissue engineering of the aortic heart valve: fundamentals and developments*. Nova Science Publishers New York, 2012.
- [13] “Aortic Valve Stenosis Topic Review.” <https://www.healio.com/cardiology/learn-the-heart/cardiology-review/topic-reviews/aortic-stenosis/introduction-and-etiology> (accessed Jun. 22, 2022).
- [14] H. Baumgartner *et al.*, “Recommendations on the echocardiographic assessment of aortic valve stenosis: a focused update from the European Association of Cardiovascular Imaging and the American Society of Echocardiography,” *European Heart Journal-Cardiovascular Imaging*, vol. 18, no. 3, pp. 254–275, 2017.
- [15] D. Horstkotte and F. Loogen, “The natural history of aortic valve stenosis,” *European Heart Journal*, vol. 9, no. suppl\_E, pp. 57–64, Apr. 1988, doi: 10.1093/eurheartj/9.suppl\_E.57.
- [16] B. H. Grimard and J. M. Larson, “Aortic Stenosis: Diagnosis and Treatment,” *afp*, vol. 78, no. 6, pp. 717–724, Sep. 2008.
- [17] B. A. Carabello and W. J. Paulus, “Aortic stenosis,” *The lancet*, vol. 373, no. 9667, pp. 956–966, 2009.
- [18] J. C. Davila, R. G. Trout, J. E. Sunner, and R. P. Glover, “A simple mechanical pulse duplicator for cinematography of cardiac valves in action,” *Ann Surg*, vol. 143, no. 4, pp. 544–551, Apr. 1956, doi: 10.1097/00000658-195604000-00017.
- [19] V. O. Björk, F. Intonti, and A. Meissl, “A Mechanical Pulse Duplicator for Testing Prosthetic Mitral and Aortic Valves,” *Thorax*, vol. 17, no. 3, pp. 280–283, Sep. 1962.
- [20] J. F. Cornhill, “An aortic-left ventricular pulse duplicator used in testing prosthetic aortic heart valves,” *The Journal of thoracic and cardiovascular surgery*, vol. 73, no. 4, pp. 550–558, 1977.
- [21] A. Mashari *et al.*, “Hemodynamic Testing of Patient-Specific Mitral Valves Using a Pulse Duplicator: A Clinical Application of Three-Dimensional Printing,” *Journal of Cardiothoracic and Vascular Anesthesia*, vol. 30, no. 5, pp. 1278–1285, Oct. 2016, doi: 10.1053/j.jvca.2016.01.013.
- [22] R. Ott *et al.*, “Development of an experimental setup for the in vitro investigation of mitral valve repair devices,” *Current Directions in Biomedical Engineering*, vol. 5, no. 1, pp. 501–503, 2019.

- [23] N. Boone, J. Moore, O. Ginty, D. Bainbridge, M. Eskandari, and T. Peters, “A dynamic mitral valve simulator for surgical training and patient specific preoperative planning,” in *Medical Imaging 2019: Image-Guided Procedures, Robotic Interventions, and Modeling*, 2019, vol. 10951, p. 109510H.
- [24] O. K. Ginty *et al.*, “Dynamic, patient-specific mitral valve modelling for planning transcatheter repairs,” *International journal of computer assisted radiology and surgery*, vol. 14, no. 7, pp. 1227–1235, 2019.
- [25] B. Moore and L. P. Dasi, “Spatiotemporal complexity of the aortic sinus vortex,” *Experiments in fluids*, vol. 55, no. 7, pp. 1–12, 2014.
- [26] H. Hatoum, B. L. Moore, P. Maureira, J. Dollery, J. A. Crestanello, and L. P. Dasi, “Aortic sinus flow stasis likely in valve-in-valve transcatheter aortic valve implantation,” *The Journal of thoracic and cardiovascular surgery*, vol. 154, no. 1, pp. 32–43, 2017.
- [27] H. Hatoum, S. M. Lilly, J. Crestanello, and L. P. Dasi, “A case study on implantation strategies to mitigate coronary obstruction in a patient receiving transcatheter aortic valve replacement,” *Journal of biomechanics*, vol. 89, pp. 115–118, 2019.
- [28] R. J. Brewer, J. D. Deck, B. Capati, and S. P. Nolan, “The dynamic aortic root: its role in aortic valve function,” *The Journal of thoracic and cardiovascular surgery*, vol. 72, no. 3, pp. 413–417, 1976.
- [29] H. Hatoum, F. Heim, and L. P. Dasi, “Stented valve dynamic behavior induced by polyester fiber leaflet material in transcatheter aortic valve devices,” *Journal of the mechanical behavior of biomedical materials*, vol. 86, pp. 232–239, 2018.
- [30] H. Hatoum and L. P. Dasi, “Spatiotemporal complexity of the aortic sinus vortex as a function of leaflet calcification,” *Annals of biomedical engineering*, vol. 47, no. 4, pp. 1116–1128, 2019.
- [31] Z. Keshavarz-Motamed *et al.*, “Effect of coarctation of the aorta and bicuspid aortic valve on flow dynamics and turbulence in the aorta using particle image velocimetry,” *Experiments in fluids*, vol. 55, no. 3, pp. 1–16, 2014.
- [32] T. Linde, K. F. Hamilton, E. C. Navalon, T. Schmitz-Rode, and U. Steinseifer, “Aortic root compliance influences hemolysis in mechanical heart valve prostheses: an in-vitro study,” *The International journal of artificial organs*, vol. 35, no. 7, pp. 495–502, 2012.

- [33] M. Kuetting *et al.*, “In vitro assessment of the influence of aortic annulus ovality on the hydrodynamic performance of self-expanding transcatheter heart valve prostheses,” *Journal of biomechanics*, vol. 47, no. 5, pp. 957–965, 2014.
- [34] C. Papolla, A. Darwish, L. Kadem, and R. Rieu, “Impact of Mitral Regurgitation on the Flow in a Model of a Left Ventricle,” *Cardiovascular Engineering and Technology*, vol. 11, no. 6, pp. 708–718, 2020.
- [35] A. Kheradvar, J. Kasalko, D. Johnson, and M. Gharib, “An in vitro study of changing profile heights in mitral bioprostheses and their influence on flow,” *Asaio Journal*, vol. 52, no. 1, pp. 34–38, 2006.
- [36] A. Kheradvar and M. Gharib, “Influence of ventricular pressure drop on mitral annulus dynamics through the process of vortex ring formation,” *Annals of biomedical engineering*, vol. 35, no. 12, pp. 2050–2064, 2007.
- [37] A. Falahatpisheh and A. Kheradvar, “High-speed particle image velocimetry to assess cardiac fluid dynamics in vitro: From performance to validation,” *European Journal of Mechanics - B/Fluids*, vol. 35, pp. 2–8, Sep. 2012, doi: 10.1016/j.euromechflu.2012.01.019.
- [38] A. Kheradvar, M. Milano, and M. Gharib, “Correlation between vortex ring formation and mitral annulus dynamics during ventricular rapid filling,” *Asaio Journal*, vol. 53, no. 1, pp. 8–16, 2007.
- [39] A. Kheradvar *et al.*, “Echocardiographic particle image velocimetry: a novel technique for quantification of left ventricular blood vorticity pattern,” *Journal of the American Society of Echocardiography*, vol. 23, no. 1, pp. 86–94, 2010.
- [40] A. Darwish, G. Di Labbio, W. Saleh, and L. Kadem, “Proper Orthogonal Decomposition Analysis of the Flow Downstream of a Dysfunctional Bileaflet Mechanical Aortic Valve,” *Cardiovascular Engineering and Technology*, pp. 1–14, 2021.
- [41] K. Vahidkhah *et al.*, “Valve thrombosis following transcatheter aortic valve replacement: significance of blood stasis on the leaflets,” *European Journal of Cardio-Thoracic Surgery*, vol. 51, no. 5, pp. 927–935, 2017.
- [42] A. N. Azadani *et al.*, “Energy loss due to paravalvular leak with transcatheter aortic valve implantation,” *The Annals of thoracic surgery*, vol. 88, no. 6, pp. 1857–1863, 2009.

- [43] N. Mirvakili, G. Di Labbio, W. Saleh, and L. Kadem, “Flow characteristics in a model of a left ventricle in the presence of a dysfunctional mitral mechanical heart valve,” *Journal of Visualization*, vol. 23, no. 1, pp. 1–8, 2020.
- [44] I. U. Okafor, A. Santhanakrishnan, B. D. Chaffins, L. Mirabella, J. N. Oshinski, and A. P. Yoganathan, “Cardiovascular magnetic resonance compatible physical model of the left ventricle for multi-modality characterization of wall motion and hemodynamics,” *Journal of Cardiovascular Magnetic Resonance*, vol. 17, no. 1, pp. 1–12, 2015.
- [45] L. M. Jennings, A. El-Gatit, Z. L. Nagy, J. Fisher, P. G. Walker, and K. G. Watterson, “Hydrodynamic function of the second-generation mitroflow pericardial bioprosthesis,” *The Annals of Thoracic Surgery*, vol. 74, no. 1, pp. 63–68, Jul. 2002, doi: 10.1016/S0003-4975(02)03617-2.
- [46] F. Viola, E. Jermyn, J. Warnock, G. Querzoli, and R. Verzicco, “Left ventricular hemodynamics with an implanted assist device: an in vitro fluid dynamics study,” *Annals of biomedical engineering*, vol. 47, no. 8, pp. 1799–1814, 2019.
- [47] B. Rahmani *et al.*, “In vitro hydrodynamic assessment of a new transcatheter heart valve concept (the TRISKELE),” *Journal of cardiovascular translational research*, vol. 10, no. 2, pp. 104–115, 2017.
- [48] S. Annerel, T. Claessens, J. Degroote, P. Segers, and J. Vierendeels, “Validation of a numerical FSI simulation of an aortic BMHV by in vitro PIV experiments,” *Medical engineering & physics*, vol. 36, no. 8, pp. 1014–1023, 2014.
- [49] P. Ferraiuoli *et al.*, “Full-field analysis of epicardial strain in an in vitro porcine heart platform,” *Journal of the mechanical behavior of biomedical materials*, vol. 91, pp. 294–300, 2019.
- [50] A. M. Leopaldi *et al.*, “In vitro hemodynamics and valve imaging in passive beating hearts,” *Journal of Biomechanics*, vol. 45, no. 7, pp. 1133–1139, Apr. 2012, doi: 10.1016/j.jbiomech.2012.02.007.
- [51] G. Querzoli, S. Fortini, S. Espa, and S. Melchionna, “A laboratory model of the aortic root flow including the coronary arteries,” *Experiments in Fluids*, vol. 57, no. 8, pp. 1–9, 2016.
- [52] A. Kheradvar and M. Gharib, “On mitral valve dynamics and its connection to early diastolic flow,” *Annals of biomedical engineering*, vol. 37, no. 1, pp. 1–13, 2009.

- [53] R. Klabunde, *Cardiovascular physiology concepts*. Lippincott Williams & Wilkins, 2011.
- [54] D. E. O. Dewi, Y. W. Hau, A. Z. M. Khudzari, I. I. Muhamad, and E. Supriyanto, Eds., *Cardiovascular Engineering: Technological Advancements, Reviews, and Applications*. Springer Singapore, 2020. doi: 10.1007/978-981-10-8405-8.
- [55] M. K. Sharp and R. K. Dharmalingham, “Development of a hydraulic model of the human systemic circulation.,” *ASAIO Journal (American Society for Artificial Internal Organs: 1992)*, vol. 45, no. 6, pp. 535–540, 1999.
- [56] F. M. Donovan, “Design of a hydraulic analog of the circulatory system for evaluating artificial hearts,” *Biomaterials, medical devices, and artificial organs*, vol. 3, no. 4, pp. 439–449, 1975.
- [57] S. Anwaruddin, J. M. Martin, J. C. Stephens, and A. T. Askari, *Cardiovascular hemodynamics: an introductory guide*. Springer Science & Business Media, 2012.
- [58] B. J. Hunt, L. Poston, A. W. Halliday, and M. Schachter, *An introduction to vascular biology: from basic science to clinical practice*. Cambridge University Press, 2002.
- [59] Z. Keshavarz-Motamed, “A diagnostic, monitoring, and predictive tool for patients with complex valvular, vascular and ventricular diseases,” *Sci Rep*, vol. 10, no. 1, Art. no. 1, Apr. 2020, doi: 10.1038/s41598-020-63728-8.
- [60] J. H. Lee *et al.*, “Fluid–structure interaction models of bioprosthetic heart valve dynamics in an experimental pulse duplicator,” *Annals of biomedical engineering*, vol. 48, no. 5, pp. 1475–1490, 2020.
- [61] H. Saaid *et al.*, “Tomographic PIV in a model of the left ventricle: 3D flow past biological and mechanical heart valves,” *Journal of biomechanics*, vol. 90, pp. 40–49, 2019.
- [62] J. P. ACHILLES and G. W. WITHROW, “Cardiovascular Physiology.” Philadelphia, 2013.
- [63] K. Davis, Jacobus. H. Muller, C. J. Meyer, and F. E. Smit, “Evaluating the impact of air compliance chamber volumes on valve performance for three different heart valves,” in *2018 3rd Biennial South African Biomedical Engineering Conference (SAIBMEC)*, Apr. 2018, pp. 1–4. doi: 10.1109/SAIBMEC.2018.8363178.
- [64] J. H. Lee, L. N. Scotten, R. Hunt, T. G. Caranasos, J. P. Vavalle, and B. E. Griffith, “Bioprosthetic aortic valve diameter and thickness are directly related to leaflet

- fluttering: Results from a combined experimental and computational modeling study,” *JTCVS Open*, vol. 6, pp. 60–81, Jun. 2021, doi: 10.1016/j.xjon.2020.09.002.
- [65] M. Grigioni *et al.*, “Pathological Patient in Protocol Definition for Bench Testing of Mechanical Cardiac Support System,” *Int J Artif Organs*, vol. 26, no. 1, pp. 64–72, Jan. 2003, doi: 10.1177/039139880302600110.
- [66] M. J. Paulsen *et al.*, “Modeling conduit choice for valve-sparing aortic root replacement on biomechanics with a 3-dimensional–printed heart simulator,” *The Journal of thoracic and cardiovascular surgery*, vol. 158, no. 2, pp. 392–403, 2019.
- [67] P. K. Kundu and I. M. Cohen, *Fluid Mechanics*. Academic Press, 2010.
- [68] L. Marx, J. A. Niestrawska, M. A. Gsell, F. Caforio, G. Plank, and C. M. Augustin, “Efficient identification of myocardial material parameters and the stress-free reference configuration for patient-specific human heart models,” *arXiv preprint arXiv:2101.04411*, 2021.
- [69] S.-J. Yoo *et al.*, “3D printing in medicine of congenital heart diseases,” *3D Printing in Medicine*, vol. 2, no. 1, pp. 1–12, 2016.
- [70] A. Gallarello *et al.*, “Patient-Specific Aortic Phantom With Tunable Compliance,” *Journal of Engineering and Science in Medical Diagnostics and Therapy*, vol. 2, no. 4, 2019.
- [71] P. H. Geoghegan, N. A. Buchmann, C. J. T. Spence, S. Moore, and M. Jermy, “Fabrication of rigid and flexible refractive-index-matched flow phantoms for flow visualisation and optical flow measurements,” *Experiments in fluids*, vol. 52, no. 5, pp. 1331–1347, 2012.
- [72] M. Büsen *et al.*, “Development of an in vitro PIV setup for preliminary investigation of the effects of aortic compliance on flow patterns and hemodynamics,” *Cardiovascular engineering and technology*, vol. 8, no. 3, pp. 368–377, 2017.
- [73] S. Marconi *et al.*, “A compliant aortic model for in vitro simulations: design and manufacturing process,” *Medical engineering & physics*, vol. 59, pp. 21–29, 2018.
- [74] K. Qiu *et al.*, “3D printed organ models with physical properties of tissue and integrated sensors,” *Advanced materials technologies*, vol. 3, no. 3, p. 1700235, 2018.

- [75] G. Haghtashtiani *et al.*, “3D printed patient-specific aortic root models with internal sensors for minimally invasive applications,” *Science Advances*, vol. 6, no. 35, p. eabb4641, Aug. 2020, doi: 10.1126/sciadv.abb4641.
- [76] K. Qiu, G. Haghtashtiani, and M. C. McAlpine, “3D printed organ models for surgical applications,” *Annual Review of Analytical Chemistry*, vol. 11, pp. 287–306, 2018.
- [77] J. M. R. S. Tavares and J. R. M. Natal, *Computational Modelling of Objects Represented in Images. Fundamentals, Methods and Applications: Proceedings of the International Symposium CompIMAGE 2006 (Coimbra, Portugal, 20-21 October 2006)*. CRC Press, 2018.
- [78] V. Sadri, I. D. Madukauwa-David, and A. P. Yoganathan, “In vitro evaluation of a new aortic valved conduit,” *The Journal of thoracic and cardiovascular surgery*, 2019.
- [79] B. L. Moore and L. P. Dasi, “Coronary flow impacts aortic leaflet mechanics and aortic sinus hemodynamics,” *Annals of biomedical engineering*, vol. 43, no. 9, pp. 2231–2241, 2015.
- [80] P. S. Gunning, N. Saikrishnan, L. M. McNamara, and A. P. Yoganathan, “An in vitro evaluation of the impact of eccentric deployment on transcatheter aortic valve hemodynamics,” *Annals of biomedical engineering*, vol. 42, no. 6, pp. 1195–1206, 2014.
- [81] F. Hegner and C. Brücker, “Combined TR-PIV and micro-pillar Wall Shear-Stress imaging in the aortic root,” 2016.
- [82] F. Hegner, D. Hess, and C. Brücker, “Volumetric 3D PIV in heart valve flow,” 2015.
- [83] Q. Li, F. Hegner, and C. H. Bruecker, “Comparative study of wall-shear stress at the ascending aorta for different mechanical heart valve prostheses,” *Journal of biomechanical engineering*, vol. 142, no. 1, 2020.
- [84] R. Zhang and Y. Zhang, “Experimental analysis of pulsatile flow characteristics in prosthetic aortic valve models with stenosis,” *Medical engineering & physics*, vol. 79, pp. 10–18, 2020.
- [85] Z. Keshavarz-Motamed, J. Garcia, N. Maftoon, E. Bedard, P. Chetaille, and L. Kadem, “A new approach for the evaluation of the severity of coarctation of the aorta using Doppler velocity index and effective orifice area: in vitro validation and

- clinical implications,” *Journal of biomechanics*, vol. 45, no. 7, pp. 1239–1245, 2012.
- [86] Z. Keshavarz-Motamed, J. Garcia, and L. Kadem, “Fluid dynamics of coarctation of the aorta and effect of bicuspid aortic valve,” *PLoS one*, vol. 8, no. 8, p. e72394, 2013.
- [87] A. Marro, T. Bandukwala, and W. Mak, “Three-dimensional printing and medical imaging: a review of the methods and applications,” *Current problems in diagnostic radiology*, vol. 45, no. 1, pp. 2–9, 2016.
- [88] Vukicevic Marija *et al.*, “Patient-Specific 3-Dimensional Printed Modeling of the Tricuspid Valve for MitraClip Procedure Planning,” *Circulation: Cardiovascular Imaging*, vol. 13, no. 7, p. e010376, Jul. 2020, doi: 10.1161/CIRCIMAGING.119.010376.
- [89] A. Vegas, “Three-dimensional transesophageal echocardiography: Principles and clinical applications,” *Annals of cardiac anaesthesia*, vol. 19, no. Suppl 1, p. S35, 2016.
- [90] Y. Fan, R. H. Wong, and A. P.-W. Lee, “Three-dimensional printing in structural heart disease and intervention,” *Annals of translational medicine*, vol. 7, no. 20, 2019.
- [91] K. M. Farooqi and P. P. Sengupta, “Echocardiography and three-dimensional printing: sound ideas to touch a heart,” *Journal of the American Society of Echocardiography*, vol. 28, no. 4, pp. 398–403, 2015.
- [92] M. Kruttschnitt, N. N. Hassan, K. Tiemann, N. Hitschrich, R. Sodian, and T. C. Lueth, “Patient-Specific Mitral Valve Replicas for Preoperative Planning of Mitral Valve Repair,” presented at the ASME 2019 International Mechanical Engineering Congress and Exposition, Jan. 2020. doi: 10.1115/IMECE2019-10347.
- [93] A. Ilina *et al.*, “Patient-specific pediatric silicone heart valve models based on 3D ultrasound,” in *Medical Imaging 2017: Image-Guided Procedures, Robotic Interventions, and Modeling*, 2017, vol. 10135, p. 1013516.
- [94] I. Gibson *et al.*, “The use of rapid prototyping to assist medical applications,” *Rapid Prototyping Journal*, vol. 12, no. 1, pp. 53–58, Jan. 2006, doi: 10.1108/13552540610637273.
- [95] J. Lantz *et al.*, “Impact of prosthetic mitral valve orientation on the ventricular flow field: Comparison using patient-specific computational fluid dynamics,” *Journal of*

- Biomechanics*, vol. 116, p. 110209, Feb. 2021, doi: 10.1016/j.jbiomech.2020.110209.
- [96] J. Lantz *et al.*, “Intracardiac flow at 4D CT: comparison with 4D flow MRI,” *Radiology*, vol. 289, no. 1, pp. 51–58, 2018.
- [97] D. Tang *et al.*, “Patient-Specific MRI-Based Right Ventricle Models Using Different Zero-Load Diastole and Systole Geometries for Better Cardiac Stress and Strain Calculations and Pulmonary Valve Replacement Surgical Outcome Predictions,” *PLOS ONE*, vol. 11, no. 9, p. e0162986, Sep. 2016, doi: 10.1371/journal.pone.0162986.
- [98] V.-T. Nguyen, C. J. Loon, H. H. Nguyen, Z. Liang, and H. L. Leo, “A semi-automated method for patient-specific computational flow modelling of left ventricles,” *Computer Methods in Biomechanics and Biomedical Engineering*, vol. 18, no. 4, pp. 401–413, Mar. 2015, doi: 10.1080/10255842.2013.803534.
- [99] H. Hatoum, A. Yousefi, S. Lilly, P. Maureira, J. Crestanello, and L. P. Dasi, “An in vitro evaluation of turbulence after transcatheter aortic valve implantation,” *The Journal of thoracic and cardiovascular surgery*, vol. 156, no. 5, pp. 1837–1848, 2018.
- [100] S. Morganti *et al.*, “Patient-specific isogeometric structural analysis of aortic valve closure,” *Computer Methods in Applied Mechanics and Engineering*, vol. 284, pp. 508–520, Feb. 2015, doi: 10.1016/j.cma.2014.10.010.
- [101] C. Manopoulos *et al.*, “Reconstruction, processing and smoothing of surface geometry of a patient specific ascending aortic aneurysm,” *IOP Conf. Ser.: Mater. Sci. Eng.*, vol. 1037, no. 1, p. 012020, Feb. 2021, doi: 10.1088/1757-899X/1037/1/012020.
- [102] M. Grab *et al.*, “Development and Evaluation of 3D-Printed Cardiovascular Phantoms for Interventional Planning and Training,” *Journal of Visualized Experiments: Jove*, no. 167, 2021.
- [103] J. M. Otton, N. S. Birbara, T. Hussain, G. Greil, T. A. Foley, and N. Pather, “3D printing from cardiovascular CT: a practical guide and review,” *Cardiovascular diagnosis and therapy*, vol. 7, no. 5, p. 507, 2017.
- [104] B. Wu, Y. Fang, and X. Lai, “Left ventricle automatic segmentation in cardiac MRI using a combined CNN and U-net approach,” *Computerized Medical Imaging and Graphics*, vol. 82, p. 101719, Jun. 2020, doi: 10.1016/j.compmedimag.2020.101719.

- [105] Anupama Bhan, Disha Bathla, and Ayush Goyal, “Patient-Specific Cardiac Computational Modeling Based on Left Ventricle Segmentation from Magnetic Resonance Images,” in *Proceedings of the International Conference on Data Engineering and Communication Technology*, Singapore, 2017, pp. 179–187. doi: 10.1007/978-981-10-1678-3\_17.
- [106] T. M. Bücking, E. R. Hill, J. L. Robertson, E. Maneas, A. A. Plumb, and D. I. Nikitichev, “From medical imaging data to 3D printed anatomical models,” *PloS one*, vol. 12, no. 5, p. e0178540, 2017.
- [107] A. M. Walker, J. Scott, D. E. Rival, and C. R. Johnston, “In vitro post-stenotic flow quantification and validation using echo particle image velocimetry (Echo PIV),” *Experiments in fluids*, vol. 55, no. 10, pp. 1–16, 2014.
- [108] H.-B. Kim, J. Hertzberg, C. Lanning, and R. Shandas, “Noninvasive measurement of steady and pulsating velocity profiles and shear rates in arteries using echo PIV: in vitro validation studies,” *Annals of biomedical engineering*, vol. 32, no. 8, pp. 1067–1076, 2004.
- [109] A. P. Narata *et al.*, “A clinically aligned experimental approach for quantitative characterization of patient-specific cardiovascular models,” *AIP Advances*, vol. 10, no. 4, p. 045106, 2020.
- [110] M. Weber *et al.*, “Multiple-step injection molding for fibrin-based tissue-engineered heart valves,” *Tissue Engineering Part C: Methods*, vol. 21, no. 8, pp. 832–840, 2015.
- [111] Y. Nakayama *et al.*, “In Body Tissue-engineered Heart Valve (Biovalve) Architecture Based on 3D Printer Molding.” Am Heart Assoc, 2013.
- [112] M. Baba *et al.*, “Development of a tailored thyroid gland phantom for fine-needle aspiration cytology by three-dimensional printing,” *Journal of surgical education*, vol. 74, no. 6, pp. 1039–1046, 2017.
- [113] N. Kadoya *et al.*, “Evaluation of deformable image registration between external beam radiotherapy and HDR brachytherapy for cervical cancer with a 3D-printed deformable pelvis phantom,” *Medical physics*, vol. 44, no. 4, pp. 1445–1455, 2017.
- [114] C. C. Ploch, C. S. Mansi, J. Jayamohan, and E. Kuhl, “Using 3D printing to create personalized brain models for neurosurgical training and preoperative planning,” *World neurosurgery*, vol. 90, pp. 668–674, 2016.

- [115] C. A. Meyer, E. Bertrand, O. Boiron, and V. Deplano, “Stereoscopically observed deformations of a compliant abdominal aortic aneurysm model,” *Journal of biomechanical engineering*, vol. 133, no. 11, 2011.
- [116] J. Voorneveld *et al.*, “High frame rate ultrasound particle image velocimetry for estimating high velocity flow patterns in the left ventricle,” *IEEE transactions on ultrasonics, ferroelectrics, and frequency control*, vol. 65, no. 12, pp. 2222–2232, 2017.
- [117] J. Voorneveld *et al.*, “4-D echo-particle image velocimetry in a left ventricular phantom,” *Ultrasound in medicine & biology*, vol. 46, no. 3, pp. 805–817, 2020.
- [118] T. Yano, M. Funayama, S. Sudo, and Y. Mitamura, “Analysis of flow within a left ventricle model fully assisted with continuous flow through the aortic valve,” *Artificial organs*, vol. 36, no. 8, pp. 714–723, 2012.
- [119] Z. Trawiński *et al.*, “Assessment of left ventricle phantom wall compressibility by ultrasound and computed tomography methods,” *Hydroacoustics*, vol. 17, 2014.
- [120] P. A. G. Morais, “Development of a patient-specific phantom model.” Doctoral program in Biomedical Engineering, 2015.
- [121] N. M. Patel and R. K. Birla, “The bioengineered cardiac left ventricle,” *Asaio Journal*, vol. 64, no. 1, pp. 56–62, 2018.
- [122] C. Vannelli, J. Moore, J. McLeod, D. Ceh, and T. Peters, “Dynamic heart phantom with functional mitral and aortic valves,” in *Medical Imaging 2015: Image-Guided Procedures, Robotic Interventions, and Modeling*, 2015, vol. 9415, p. 941503.
- [123] C. Lueders, B. Jastram, R. Hetzer, and H. Schwandt, “Rapid manufacturing techniques for the tissue engineering of human heart valves,” *European Journal of Cardio-Thoracic Surgery*, vol. 46, no. 4, pp. 593–601, 2014.
- [124] A. Razavykia, E. Brusa, C. Delprete, and R. Yavari, “An Overview of Additive Manufacturing Technologies—A Review to Technical Synthesis in Numerical Study of Selective Laser Melting,” *Materials*, vol. 13, no. 17, p. 3895, 2020.
- [125] N. Alves *et al.*, “Cardiac tissue-mimicking ballistic gel phantom for ultrasound imaging in clinical and research applications,” *Ultrasound in Medicine & Biology*, vol. 46, no. 8, pp. 2057–2069, 2020.
- [126] A. Henn, S. Callahan, M. Kendrick, A. Kheradvar, and A. A. Amini, “An MR compatible aortic arch phantom with calcific polymeric valves,” in *Medical*

*Imaging 2019: Biomedical Applications in Molecular, Structural, and Functional Imaging*, 2019, vol. 10953, p. 109531L.

- [127] E. Vignali *et al.*, “Design, simulation, and fabrication of a three-dimensional printed pump mimicking the left ventricle motion,” *The International journal of artificial organs*, vol. 42, no. 10, pp. 539–547, 2019.
- [128] N. M. Patel, “Bioengineering A Three-Dimensional Cardiac Left Ventricle,” PhD Thesis, 2015.
- [129] I. W. W. Lau and Z. Sun, “Dimensional Accuracy and Clinical Value of 3D Printed Models in Congenital Heart Disease: A Systematic Review and Meta-Analysis,” *Journal of Clinical Medicine*, vol. 8, no. 9, Art. no. 9, Sep. 2019, doi: 10.3390/jcm8091483.
- [130] P. Bhatla, J. T. Tretter, S. Chikkabyrappa, S. Chakravarti, and R. S. Mosca, “Surgical planning for a complex double-outlet right ventricle using 3D printing,” *Echocardiography*, vol. 34, no. 5, pp. 802–804, 2017, doi: <https://doi.org/10.1111/echo.13512>.
- [131] E. Ferrari *et al.*, “Three-dimensional printing in adult cardiovascular medicine for surgical and transcatheter procedural planning, teaching and technological innovation,” *Interactive CardioVascular and Thoracic Surgery*, vol. 30, no. 2, pp. 203–214, Feb. 2020, doi: 10.1093/icvts/ivz250.
- [132] K. W. Riggs, G. Dsouza, J. T. Broderick, R. A. Moore, and D. L. S. Morales, “3D-printed models optimize preoperative planning for pediatric cardiac tumor debulking,” *Translational Pediatrics*, vol. 7, no. 3, Art. no. 3, Jul. 2018.
- [133] I. Abudayyeh, B. Gordon, M. M. Ansari, K. Jutzy, L. Stoletniy, and A. Hilliard, “A practical guide to cardiovascular 3D printing in clinical practice: Overview and examples,” *Journal of Interventional Cardiology*, vol. 31, no. 3, pp. 375–383, 2018, doi: <https://doi.org/10.1111/joic.12446>.
- [134] I. Lau and Z. Sun, “Three-dimensional printing in congenital heart disease: A systematic review,” *Journal of Medical Radiation Sciences*, vol. 65, no. 3, pp. 226–236, 2018, doi: <https://doi.org/10.1002/jmrs.268>.
- [135] R. Wilhite and I. Wölfel, “3D Printing for veterinary anatomy: An overview,” *Anatomia, Histologia, Embryologia*, vol. 48, no. 6, pp. 609–620, 2019, doi: <https://doi.org/10.1111/ahe.12502>.

- [136] A. Anastasiou, C. Tsirmpas, A. Rompas, K. Giokas, and D. Koutsouris, “3D printing: Basic concepts mathematics and technologies,” in *13th IEEE International Conference on BioInformatics and BioEngineering*, 2013, pp. 1–4.
- [137] N. Jones, “Science in three dimensions: the print revolution,” *Nature News*, vol. 487, no. 7405, p. 22, 2012.
- [138] A. A. Giannopoulos, D. Mitsouras, S.-J. Yoo, P. P. Liu, Y. S. Chatzizisis, and F. J. Rybicki, “Applications of 3D printing in cardiovascular diseases,” *Nat Rev Cardiol*, vol. 13, no. 12, pp. 701–718, Dec. 2016, doi: 10.1038/nrcardio.2016.170.
- [139] B. Mosadegh, G. Xiong, S. Dunham, and J. K. Min, “Current progress in 3D printing for cardiovascular tissue engineering,” *Biomedical Materials*, vol. 10, no. 3, p. 034002, 2015.
- [140] J. Hiemenz, “3D printing with FDM: How it Works,” *Stratasys Inc*, vol. 1, pp. 1–5, 2011.
- [141] A. C. de Bruijn, G. Gómez-Gras, and M. A. Pérez, “Mechanical study on the impact of an effective solvent support-removal methodology for FDM Ultem 9085 parts,” *Polymer Testing*, vol. 85, p. 106433, 2020.
- [142] C. Xu, J. Liang, and J. Yang, “History of Cardiovascular 3D Printing,” in *Cardiovascular 3D Printing*, Springer, 2021, pp. 1–2.
- [143] S. F. S. Shirazi *et al.*, “A review on powder-based additive manufacturing for tissue engineering: selective laser sintering and inkjet 3D printing,” *Science and technology of advanced materials*, 2015.
- [144] A. Awad, F. Fina, A. Goyanes, S. Gaisford, and A. W. Basit, “3D printing: Principles and pharmaceutical applications of selective laser sintering,” *International Journal of Pharmaceutics*, vol. 586, p. 119594, 2020.
- [145] B. Derby, “Inkjet printing of functional and structural materials: fluid property requirements, feature stability, and resolution,” *Annual Review of Materials Research*, vol. 40, pp. 395–414, 2010.
- [146] P. Ding, L. Li, M. Yang, and J. Yang, “The Methods of Cardiovascular 3D Printing,” in *Cardiovascular 3D Printing*, Springer, 2021, pp. 3–14.
- [147] C. Pastia, “3D Printing of Buildings. Limits, Design, Advantages and Disadvantages. Could This Technique Contribute to Sustainability of Future Buildings?,” *CRITICAL THINKING IN THE SUSTAINABLE REHABILITATION AND RISK MANAGEMENT OF*, p. 298, 2020.

- [148] H. Quan, T. Zhang, H. Xu, S. Luo, J. Nie, and X. Zhu, “Photo-curing 3D printing technique and its challenges,” *Bioactive materials*, vol. 5, no. 1, pp. 110–115, 2020.
- [149] M. Dipaola, *3D printing in orthopaedic surgery*. Elsevier Health Sciences, 2018.
- [150] D. Maragiannis *et al.*, “Replicating patient-specific severe aortic valve stenosis with functional 3D modeling,” *Circulation: Cardiovascular Imaging*, vol. 8, no. 10, p. e003626, 2015.
- [151] A. El Sabbagh *et al.*, “The various applications of 3D printing in cardiovascular diseases,” *Current cardiology reports*, vol. 20, no. 6, pp. 1–9, 2018.
- [152] S. H. Gharaie, “A Novel Design and Optimization of a Polymeric Aortic Valve using Numerical and Experimental Techniques,” PhD Thesis, Swinburne University of Technology, 2016.
- [153] Z. Keshavarz-Motamed *et al.*, “Non-Invasive Determination of Left Ventricular Workload in Patients with Aortic Stenosis Using Magnetic Resonance Imaging and Doppler Echocardiography,” *PLOS ONE*, vol. 9, no. 1, p. e86793, Jan. 2014, doi: 10.1371/journal.pone.0086793.
- [154] D. Chemla, I. Antony, Y. Lecarpentier, and A. Nitenberg, “Contribution of systemic vascular resistance and total arterial compliance to effective arterial elastance in humans,” *American Journal of Physiology-Heart and Circulatory Physiology*, vol. 285, no. 2, pp. H614–H620, 2003.
- [155] J. K. Li, *The arterial circulation: physical principles and clinical applications*. Springer Science & Business Media, 2000.
- [156] I. Standard, “ISO 5840-3: 2013 (E): Cardiovascular implants: cardiac valve prostheses. Part 3: Heart valve substitutes implanted by transcatheter techniques.” ISO Copyright Office Geneva, 2015.
- [157] K. Itatani *et al.*, “Influence of surgical arch reconstruction methods on single ventricle workload in the Norwood procedure,” *The Journal of Thoracic and Cardiovascular Surgery*, vol. 144, no. 1, pp. 130–138, Jul. 2012, doi: 10.1016/j.jtcvs.2011.08.013.
- [158] M. Thiriet, *Biology and mechanics of blood flows: Part II: Mechanics and medical aspects*. Springer Science & Business Media, 2007.
- [159] R. Sadeghi, B. Tomka, S. Khodaei, J. Garcia, J. Ganame, and Z. Keshavarz-Motamed, “Reducing Morbidity and Mortality in Patients With Coarctation

- Requires Systematic Differentiation of Impacts of Mixed Valvular Disease on Coarctation Hemodynamics,” *Journal of the American Heart Association*, vol. 11, no. 2, p. e022664, 2022.
- [160] R. Sadeghi *et al.*, “Impact of extra-anatomical bypass on coarctation fluid dynamics using patient-specific lumped parameter and Lattice Boltzmann modeling,” *Scientific Reports*, vol. 12, no. 1, pp. 1–24, 2022.
- [161] M. Kadem, L. Garber, M. Abdelkhalek, B. K. Al-Khazraji, and Z. Keshavarz-Motamed, “Hemodynamic modeling, medical imaging, and machine learning and their applications to cardiovascular interventions,” *IEEE Reviews in Biomedical Engineering*, 2022.
- [162] R. Sadeghi, N. Gasner, S. Khodaei, J. Garcia, and Z. Keshavarz-Motamed, “Impact of mixed valvular disease on coarctation hemodynamics using patient-specific lumped parameter and Lattice Boltzmann modeling,” *International Journal of Mechanical Sciences*, vol. 217, p. 107038, 2022.
- [163] L. Garber, S. Khodaei, and Z. Keshavarz-Motamed, “The critical role of lumped parameter models in patient-specific cardiovascular simulations,” *Archives of Computational Methods in Engineering*, pp. 1–24, 2021.
- [164] S. Khodaei *et al.*, “Personalized intervention cardiology with transcatheter aortic valve replacement made possible with a non-invasive monitoring and diagnostic framework,” *Scientific Reports*, vol. 11, no. 1, pp. 1–28, 2021.
- [165] M. Baiocchi *et al.*, “Effects of Choice of Medical Imaging Modalities on a Non-invasive Diagnostic and Monitoring Computational Framework for Patients With Complex Valvular, Vascular, and Ventricular Diseases Who Undergo Transcatheter Aortic Valve Replacement,” *Frontiers in Bioengineering and Biotechnology*, p. 389, 2021.
- [166] S. Khodaei, R. Sadeghi, P. Blanke, J. Leipsic, A. Emadi, and Z. Keshavarz-Motamed, “Towards a non-invasive computational diagnostic framework for personalized cardiology of transcatheter aortic valve replacement in interactions with complex valvular, ventricular and vascular disease,” *International Journal of Mechanical Sciences*, vol. 202, p. 106506, 2021.
- [167] M. Asaadi, W. Mawad, A. Djebbari, Z. Keshavarz-Motamed, N. Dahdah, and L. Kadem, “On left ventricle stroke work efficiency in children with moderate aortic valve regurgitation or moderate aortic valve stenosis,” *Pediatric Cardiology*, vol. 43, no. 1, pp. 45–53, 2022.

- [168] R. Sadeghi, S. Khodaei, J. Ganame, and Z. Keshavarz-Motamed, “towards non-invasive computational-mechanics and imaging-based diagnostic framework for personalized cardiology for coarctation,” *Scientific Reports*, vol. 10, no. 1, pp. 1–19, 2020.
- [169] Z. Keshavarz-Motamed, “A diagnostic, monitoring, and predictive tool for patients with complex valvular, vascular and ventricular diseases,” *Scientific Reports*, vol. 10, no. 1, Art. no. 1, Apr. 2020, doi: 10.1038/s41598-020-63728-8.
- [170] Z. Keshavarz-Motamed *et al.*, “Mixed valvular disease following transcatheter aortic valve replacement: quantification and systematic differentiation using clinical measurements and image-based patient-specific in silico modeling,” *Journal of the American Heart Association*, vol. 9, no. 5, p. e015063, 2020.
- [171] N. Westerhof, N. Stergiopoulos, M. I. Noble, and B. E. Westerhof, *Snapshots of hemodynamics: an aid for clinical research and graduate education*, vol. 7. Springer, 2010.
- [172] A. E. Abbas, *Aortic Stenosis: Case-Based Diagnosis and Therapy*. Springer, 2015.
- [173] W. F. Armstrong and T. Ryan, *Feigenbaum’s echocardiography*. Lippincott Williams & Wilkins, 2012.
- [174] C. M. Otto and R. O. Bonow, *Valvular Heart Disease: A Companion to Braunwald’s Heart Disease E-Book*. Elsevier Health Sciences, 2009.
- [175] L. Kadem, R. Rieu, J. G. Dumesnil, L.-G. Durand, and P. Pibarot, “Flow-dependent changes in Doppler-derived aortic valve effective orifice area are real and not due to artifact,” *Journal of the American College of Cardiology*, vol. 47, no. 1, pp. 131–137, 2006.
- [176] C. M. Otto, “Why is aortic sclerosis associated with adverse clinical outcomes?\*,” *Journal of the American College of Cardiology*, vol. 43, no. 2, pp. 176–178, Jan. 2004, doi: 10.1016/j.jacc.2003.10.027.
- [177] K. P. Owashi, A. Hubert, E. Galli, E. Donal, A. I. Hernández, and V. L. Rolle, “Model-based estimation of left ventricular pressure and myocardial work in aortic stenosis,” *PLOS ONE*, vol. 15, no. 3, p. e0229609, Mar. 2020, doi: 10.1371/journal.pone.0229609.
- [178] A. Mirnajafi, J. M. Raymer, L. R. McClure, and M. S. Sacks, “The flexural rigidity of the aortic valve leaflet in the commissural region,” *Journal of Biomechanics*, vol. 39, no. 16, pp. 2966–2973, Jan. 2006, doi: 10.1016/j.jbiomech.2005.10.026.

- [179] E. Ben-Assa *et al.*, “Ventricular stroke work and vascular impedance refine the characterization of patients with aortic stenosis,” *Science translational medicine*, vol. 11, no. 509, p. eaaw0181, 2019.
- [180] Z. Keshavarz-Motamed, J. Garcia, P. Pibarot, E. Larose, and L. Kadem, “Modeling the impact of concomitant aortic stenosis and coarctation of the aorta on left ventricular workload,” *Journal of Biomechanics*, vol. 44, no. 16, pp. 2817–2825, Nov. 2011, doi: 10.1016/j.jbiomech.2011.08.001.